

Marquette University

e-Publications@Marquette

Dissertations (2009 -)

Dissertations, Theses, and Professional
Projects

Patient-Specific Modeling of Altered Coronary Artery Hemodynamics to Predict Morbidity in Patients with Anomalous Origin of a Coronary Artery

Atefeh Razavi
Marquette University

Follow this and additional works at: https://epublications.marquette.edu/dissertations_mu



Part of the [Biomedical Engineering and Bioengineering Commons](#)

Recommended Citation

Razavi, Atefeh, "Patient-Specific Modeling of Altered Coronary Artery Hemodynamics to Predict Morbidity in Patients with Anomalous Origin of a Coronary Artery" (2020). *Dissertations (2009 -)*. 919.
https://epublications.marquette.edu/dissertations_mu/919

PATIENT-SPECIFIC MODELING OF ALTERED CORONARY ARTERY
HEMODYNAMICS TO PREDICT MORBIDITY IN PATIENTS WITH ANOMALOUS
ORIGIN OF A CORONARY ARTERY

by

Atefeh Razavi, M.S.

A Dissertation Submitted to the Faculty of the Graduate School,
Marquette University,
in Partial Fulfillment of the Requirements for
the Degree of Doctor of Philosophy

Milwaukee, Wisconsin

May 2020

ABSTRACT
PATIENT-SPECIFIC MODELING OF ALTERED CORONARY ARTERY
HEMODYNAMICS TO PREDICT MORBIDITY IN PATIENTS WITH ANOMALOUS
ORIGIN OF A CORONARY ARTERY

Atefeh Razavi, M.S.

Marquette University, 2020

Anomalous aortic origin of a coronary artery (AAOCA) is a condition where a coronary artery arises from the opposite aortic sinus, often with acute angle of origin (AO). AAOCA is associated with ischemia.¹ This is especially concerning when the anomalous coronary artery takes an intramural course within the aortic wall, creating the potential for distortion or compression. Unroofing surgery replaces a restrictive ostium and intramural segment with a large ostium from the appropriate sinus and aims to create a less acute AO. Although these anatomical features may alter coronary artery blood flow patterns, hemodynamic indices such as time averaged wall shear stress (TAWSS), oscillatory shear index (OSI) and fractional flow reserve (FFR) that impact a patient's future risk for ischemia and morbidity²⁻⁶ remain largely unexplored. We hypothesized that morphology of the anomalous coronary artery has a significant impact on local hemodynamics of AAOCA and aimed to 1) characterize hemodynamic alterations in AAOCA by patient-specific simulation of patients pre-operative and post-unroofing using advanced coronary artery boundary conditions, 2) assess the impact of AO on the severity of hemodynamic alterations, and 3) characterize the hemodynamic effect of proximal narrowing of the anomalous artery and hyperemic resistance of the downstream vasculature (HMR) on FFR. Findings from Aim 1 suggested that different flow patterns exist natively between right and left coronary arteries, a reduction in TAWSS is observed post-unroofing, and that unroofing may normalize TAWSS but with variance related to the AO. Data from Aim 2 indicated that AO alters TAWSS and OSI in simulations run from a patient-specific model with virtually rotated AOs. The arterial wall experienced lower TAWSS for more acute AO near the ostium. Distal to the ostium, arterial wall experienced higher TAWSS for more acute AO. Findings from Aim 3 showed that for a given narrowing, higher HMR resulted in higher FFR thereby mimicking the interaction of the upstream and downstream micro-vasculature resistance to regulate FFR for the first time using computational models of AAOCA. Virtual manipulation of the anomalous artery provided a direct comparison for the effect of the anatomic high-risk features. Collectively, these results serve as the foundation for larger studies of AAOCA that could correlate hemodynamics with outcomes for risk stratification and surgical evaluation.

ACKNOWLEDGMENTS

Atefeh Razavi

I have a special feeling of gratitude to my supervisor, Dr. John LaDisa, Thank you for your valuable guidance and continuous support all along. You taught me a lot about research, scientific writing and determining proper solution methodologies to optimize research findings. I would like to thank you for allowing me to grow as a researcher.

I would also like to thank you Dr. Peter Frommelt and Dr. Shagun Sachdeva. Your proposal shaped this study. Your constant help, advice and feedback were critical to the improvement of this project.

I am also grateful to you Dr. Rocky Kandail. You taught me a lot, answered all my questions patiently and gave me great tips on how to move forward with my research throughout these years.

I wish to extend my gratitude to my other committee members: Dr. Gui Garcia for your support and generously offering me to use your resources for different projects, Dr. Claudio Chiastra for your instructive advice and helpful suggestions.

Most important, I need to thank my family whose unconditional love and encouragement has given me more than I deserved. Thank you for your never-ending support and sacrifices you have made for me. Baba, Maman, Saleh and Sadegh, I am forever grateful for having and feeling you in my life.

I would also like to thank all my friends and former and current labmates. Maryam, my life-long friend, and Faraneh, you have been such treasures in my life and like the sisters I never had. Thank you for always being there for me. Sophia, thank you for being such a supportive and wonderful friend. Jesse, thank you for being nice and supportive. I will never forget your philosophical jokes. Arash and Aloma, you are talented and hardworking people and I am thankful that I had the chance to work with and learn from you.

Finally, I would like to thank the Graduate School and all the Marquette University administration.

TABLE OF CONTENTS

ACKNOWLEDGMENTS	i
ABBREVIATIONS and ACRONYMS	v
SYMBOLS.....	vii
1 BACKGROUND	1
1.1 Overview	1
1.2 Anatomy of the Coronary Artery Circulation.....	1
1.3 Physiology of the Coronary Artery Circulation.....	2
1.4 Anomalous Aortic Origin of the Coronary Artery	3
1.5 Functional and Hemodynamic Assessment of Coronary Arteries	6
1.5.1 Wall Shear Stress	7
1.5.2 Oscillatory Shear Index.....	8
1.5.3 Fractional Flow Reserve.....	9
1.5.4 Hyperemic Microvascular Resistance	11
1.6 Patient-specific CFD Modeling	12
1.7 Aims and Hypothesis.....	13
1.7.1 Hypothesis.....	13
1.7.2 Specific Aims	14
1.7.2.1 Specific Aim 1	14
1.7.2.2 Specific Aim 2	15
1.7.2.3 Specific Aim 3	15

2	MATERIALS and METHODS	17
2.1	Overview	17
2.2	Geometry Reconstruction of AAOCA Patients from MRI Data	19
2.3	Boundary Conditions.....	21
2.3.1	Inflow and Left Ventricular Pressure	21
2.3.2	Outlet Boundary Conditions.....	22
2.3.2.1	Aortic Outlet BCs.....	23
2.3.2.2	Coronary Outlets BCs	23
2.3.2.2.1	Resistance Parameters	23
2.3.2.2.2	Compliance Parameters.....	27
2.3.2.2.3	Pressure Parameters.....	28
2.4	Meshing	32
2.5	Computational Setup	35
2.6	Hemodynamics Visualization, Quantification and Statistical Analysis	36
2.7	Measurement of the Length of Intramurality, Eccentricity Index and AO.....	37
2.8	Virtual Alteration of the Angle of the Origin	39
2.9	Virtual Narrowing of the Proximal LMCA and Altering HMR	40
3	RESULTS	42
3.1	Overview	42
3.2	Morphometric Parameters of the 3D Models	42
3.3	Physiologic Flow and Pressure from Patient-Specific Boundary Conditions	45

3.4 Hemodynamic Comparison between Pre-operative and Post-unroofing States	46
3.5 Hemodynamic Comparison between Left and Right Coronary Arteries.....	49
3.6 Hemodynamic Comparison between Unroofed and Contralateral Coronary Arteries	51
3.7 Hemodynamic Comparison between Virtually Created Angles of Origins	52
3.8 FFR Analysis in Virtually Compressed Anomalous Artery	56
4 DISCUSSION	58
4.1 Overview	58
4.2 Summary of Findings from Aim 1	59
4.3 Summary of Findings from Aim 2	61
4.4 Summary of Findings from Aim 3	62
4.5 Limitations, Computational Considerations and Future Directions	63
4.6 Conclusion.....	68
BIBLIOGRAPHY	69

ABBREVIATIONS and ACRONYMS

AAOCA	Anomalous aortic origin of a coronary artery
AO	Angle of origin
BP	Blood pressure
BC	Boundary condition
CAA	Coronary artery anomaly
CAD	Coronary artery disease
CABG	Coronary artery bypass graft
CFD	Computational fluid dynamics
CFL	Courant–Friedrichs–Lewy
CMR	Cardiovascular magnetic resonance
CO	Cardiac output
CT	Computed tomography
DBP	Diastolic blood pressure
ECG	Electrocardiogram
FEM	Finite element methods
FFR	Fractional flow reserve
FFR _{CT}	Virtually derived FFR form CT
FSI	Fluid structure interaction
HMR	Hyperemic microvascular resistance
HPC	High performance computing
HSR	Hyperemic stenosis resistance
IVUS	Intravascular ultrasound
LAD	Left anterior descending
LCX	Left circumflex artery

LMCA	Left main coronary artery
LPN	Lumped parameter network
LVP	Left ventricular pressure
MBP	Mean blood pressure
MRI	Magnetic resonance imaging
OSI	Oscillatory shear index
PA	Pulmonary artery
PCI	Percutaneous coronary intervention
PC-MRI	Phase contrast MRI
RCA	Right coronary artery
ROI	Region of interest
SBP	Systolic blood pressure
SCD	Sudden cardiac death
SSFP	Steady state free precession
TAWSS	Time averaged wall shear stress
TE	Echo time
TR	Repetition time
vFFR	virtual FFR
WSS	Wall shear stress

SYMBOLS

\mathbf{a}	Vector tangent to the centerline of the proximal coronary artery
A	Ostial surface area
A_i	Area of the coronary outlet
A_{pos}	Area under the WSS vs time curve with positive WSS
A_{neg}	Area under the WSS vs time curve with negative WSS
C	Aortic compliance
C_a	Coronary arterial compliance
$C_{cor,i}$	Compliance at the coronary outlet
C_{im}	Coronary intramyocardial compliance
$C_{tot,left}$	Total left coronary compliance
$C_{tot,right}$	Total right coronary compliance
D	Diameter
μ	Viscosity
\mathbf{n}_w	Unit normal vector to the flow direction on the wall
\mathbf{N}	Normal vector to the ostial plane
P	Pressure
P_a	Aortic pressure
P_a	Pressure distal to the stenotic lesion
$P_{im,left}$	Left intramyocardial pressure
$P_{im,right}$	Right intramyocardial pressure
P_{rest}	Mean BP under resting conditions
P_{stress}	Mean BP under stress conditions
∇P	Pressure gradient

ρ	Density
R_a	Coronary arterial resistance
$R_{a,micro}$	Coronary arterial microcirculation resistance
$R_{cor,i}$	Resistance at the coronary outlet
$R_{cor,tot}$	Total coronary resistance
R_d	Distal resistance
R_p	Proximal resistance
R_v	Coronary venous resistance
$R_{v,micro}$	Coronary venous microcirculation resistance
$\boldsymbol{\tau}$	Viscous stress tensor
$\boldsymbol{\tau}_w$	Wall shear stress vector
$\nabla \cdot \boldsymbol{\tau}$	Divergence of viscous stress tensor
T	Period (i.e. cardiac cycle)
\boldsymbol{V}	Velocity vector
\vec{V}_t	Partial derivative of velocity vector with respect to time
$\nabla \boldsymbol{V}$	Velocity gradient
$\nabla \cdot \boldsymbol{V}$	Divergence of velocity
$\nabla \boldsymbol{V}^T$	Transpose of the velocity gradient

1 BACKGROUND

1.1 Overview

This study is aimed at assessing hemodynamics in patients with anomalous aortic origin of the coronary artery (AAOCA) as well as examining the impact of anatomic high-risk features. This chapter familiarizes the reader with the anatomy and physiology of the coronary artery circulation, as well as some related abnormalities with functional complications. The role of hemodynamics in the pathophysiology of the coronary artery circulation is discussed with a focus on three hemodynamic indices: wall shear stress (WSS), oscillatory shear index (OSI) and fractional flow reserve (FFR). Computational fluid dynamics (CFD) techniques capable of predicting these indices with high accuracy are introduced, and their application in cardiovascular disease are explained. More details on specific aims are presented in section 1.7

1.2 Anatomy of the Coronary Artery Circulation

The coronary arteries provide oxygenated blood to the heart. More specifically, they form a complex vascular network to provide blood and nutrients to different layers of cardiac muscle (i.e. epicardium, myocardium and endocardium). Epicardial arteries originate from the sinuses of Valsalva and course down the surface of the heart (see Figure 1.1). The origin of the coronary artery in the sinus of Valsalva is called coronary ostium. The left main coronary artery (LMCA) arises from the left sinus of Valsalva and branches into two main arteries: the left anterior descending (LAD) and the left circumflex (LCX) arteries. The LAD and LCX principally perfuse the left ventricle and left atrium. The right coronary artery (RCA) stems from the right sinus of Valsalva. The RCA mainly perfuses the right ventricle and right atrium and partially perfuses the left ventricle.

There are a large number of small arteries branching from the main epicardial vessels that spread over the epicardium or penetrate through the myocardium. The penetrating small arteries further branch into even smaller arteries known as the arterioles, which constitute the coronary microcirculation. Coronary arterioles give rise to the capillary beds where oxygen and nutrients are delivered to cardiac tissue.⁷

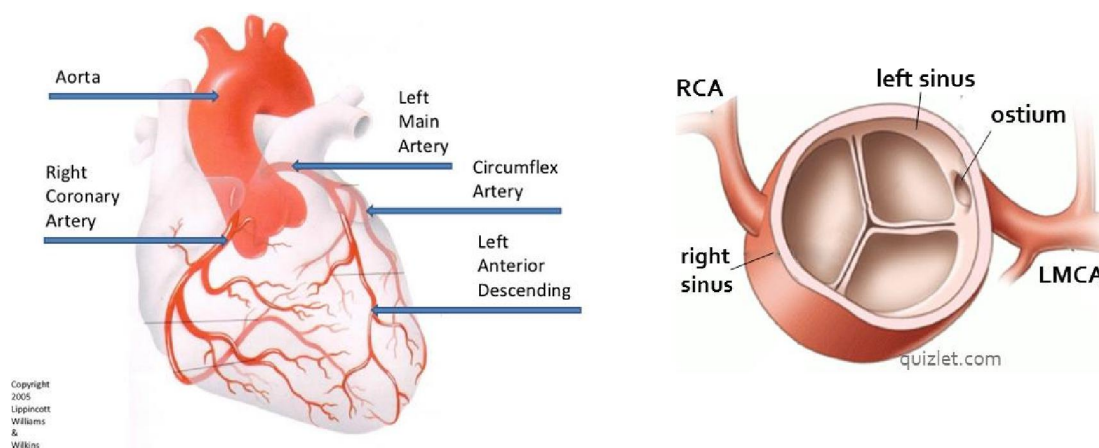


Figure 1.1 A schematic of coronary artery anatomy. Left: arterial network Right: aortic valve and sinuses of Valsalva

1.3 Physiology of the Coronary Artery Circulation

Epicardial, small arteries, arterioles and capillaries have different sizes and functions (see Figure 1.2). Large epicardial arteries are conductance vessels with small pressure drop under normal healthy conditions and are responsible for the bulk transport of oxygenated blood. Small arteries and arterioles play an important role in regulating coronary resistance through various mechanisms that control the vascular tone and diameter.⁸ Vasodilation or vasoconstriction in the small arteries is affected by the shear-dependent response to the changes in blood flow.^{8,9} Vasoactive response of the arterioles includes the metabolic response to hypoxia or strenuous activities as well as the myogenic response to changes in intraluminal pressure.

Altered vascular resistance and the subsequent changes in myocardial blood flow (coronary perfusion) affects cardiac tissue. Moreover, cardiac tissue affects myocardial blood flow that results in the so-called phasic behavior. Contraction of cardiomyocytes (cardiac muscle cells) during systole exerts a contractile force on the arteries embedded through intramyocardial pressure, which also leads to a decrease in coronary artery blood flow. During diastole, when the cardiac muscle relaxes and intramyocardial pressure is reduced, flow resumes and fills the microcirculatory arteries.¹⁰

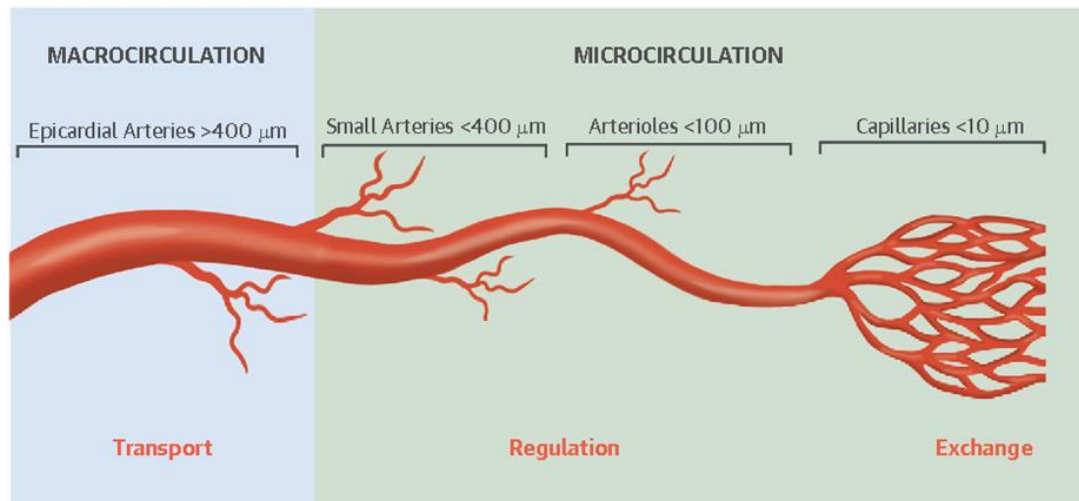


Figure 1.2 Coronary artery macro and micro-circulation size and function, adapted with permission from Bruyne et.al, 2016¹¹

1.4 Anomalous Aortic Origin of the Coronary Artery

Coronary artery anomalies (CAAs) may relate to any defect in size, shape, origin or location of the coronary arteries. Three anomalies are associated with clinical implications and may need surgical intervention. They include coronary artery fistula, coronary arterial origin from the pulmonary artery (PA) and AAOCA. These anomalies may impair coronary artery blood flow

that may ultimately result in clinical manifestations such as myocardial infarction, congestive heart failure, angina, ventricular aneurysms, or sudden cardiac death (SCD).¹²

AAOCA is a rare congenital heart anomaly, 0.35 % to 2.1 % incidence rate⁴, where the origin of a coronary artery arises from the wrong sinus of Valsalva. Although the incidence of AAOCA is relatively rare, the anomaly can place affected patients at risk for SCD.¹³ In left AAOCA, left coronary artery originates from the right sinus of Valsalva and in right AAOCA, right coronary artery originates from the left sinus of Valsalva.(Figure 1.3)

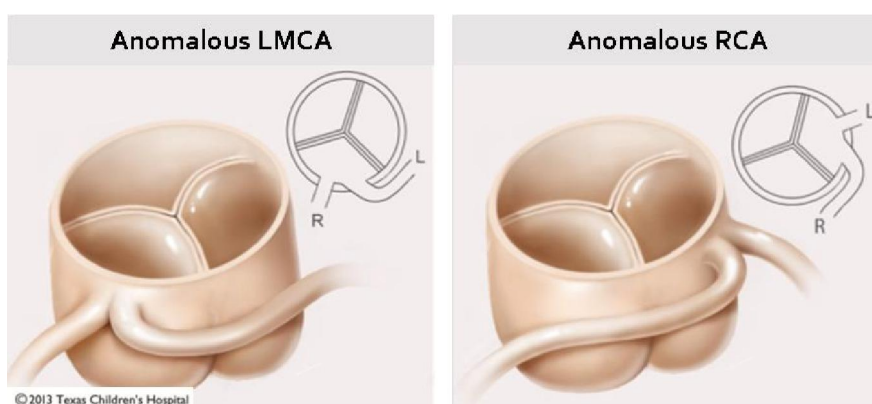


Figure 1.3 Illustration of the aortic valve in the left and right AAOCA

In interarterial AAOCA, the anomalous coronary artery follows a course between the great arteries (i.e. PA and the aorta). AAOCA is especially concerning when the anomalous coronary artery takes an intramural course within the anterior aortic wall, creating the potential for distortion or compression of the coronary segment during times of increased myocardial demand. Of note, AAOCA is the 2nd leading cause of SCD in young athletes.⁴ AAOCA can present with exertional chest pain, syncope, cardiac arrest post successful resuscitation or sudden death.¹⁴ Once identified, AAOCA may require life-long restriction from exercise because of the risk of acute myocardial ischemia.¹³

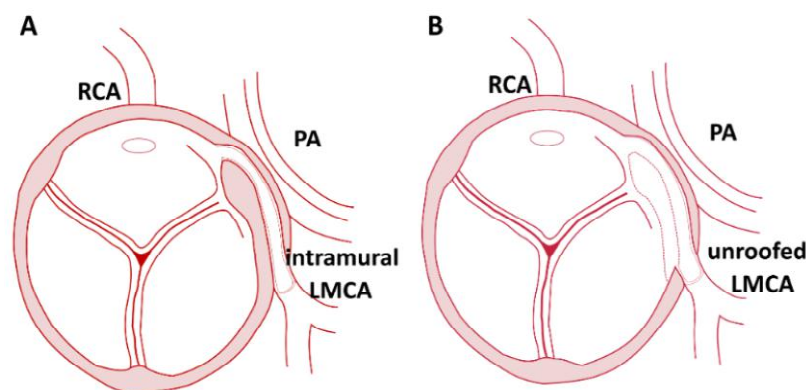


Figure 1.4 Cross-sectional drawing of the aorta and pulmonary artery for the intramural anomalous aortic origin of the left coronary artery (A) pre-operative and (B) post-unroofing

Several studies hypothesized that an acute angle of origin, (i.e. $AO < 45$ degrees¹⁵) and a potential slit-like ostium may cause diminished flow to the abnormal coronary artery with aortic root expansion.^{16,17} Intraluminal narrowing (i.e. lateral compression of the intramural course) may further limit or even obstruct the flow when the aortic root and pulmonary artery expand during stress or elevated blood flow conditions leading to the propensity for exercise-related SCD.^{18,14} However, effects of these factors on local hemodynamics remain largely unexplored. There has been only one numerical study of an idealized AAOCA geometry with aortic expansion modeled at different AOs using finite element methods (FEM), which was conducted in the absence of detailed flow patterns from CFD analysis.¹⁹ Results of this study indicated that under exercise loading conditions, expansion of the anomalous coronary arteries was impaired. The impairment occurred especially at the ostium creating an elliptical shape as a result of an acute AO.

Over the past 2 decades, a surgical technique to address intramural AAOCA-related pathology has been developed. The procedure, known as “unroofing”, removes the intramural coronary segment that runs within the aortic wall.²⁰ Surgical unroofing alters coronary anatomy and presumably removes the risk of ischemia by opening the potentially restrictive anomalous coronary ostium and intramural segment, which leads to a large patent ostium that arises

perpendicularly from appropriate aortic sinus (Figure 1.4B).²¹ Studies have shown improvement in symptoms post-operatively.²² However, there have also been recent reports of sudden cardiac arrest after surgical unroofing of AAOCA. These more recent reports raise questions about the long term consequences of the surgery and safety of AAOCA patients returning to physical activities after surgery.²³ The effects of surgical unroofing on myocardial blood flow and coronary morphology have not been investigated in detail. Based on the current data from AAOCA patients, the exact mechanism of ischemia in these patients post-operatively is unclear. Several mechanisms have been hypothesized including persistence of myocardial injury from the original anatomy/initial ischemic events prior to surgery, coronary artery distortion related to the surgery, progressive development of neo-ostial scar after unroofing that compromises coronary blood flow, and abnormal AO that limits coronary artery flow reserve and/or introduces adverse flow patterns and hemodynamics, previously linked to the onset and progression of atherosclerosis.²⁴⁻²⁶ Any continued compromise to coronary hemodynamics after unroofing may alter the patient's risk for future atherogenesis and/or myocardial ischemia. In particular, changes in local morphology from the unroofing procedure may impact coronary artery blood flow patterns by creating regions containing abnormal hemodynamic indices that have been related to the coronary vascular pathologies.^{25,27} The following section emphasizes the importance of hemodynamics and functional assessment and reviews a role for patient-specific modeling in non-invasive determination of hemodynamic indices to improve treatment management and surgical techniques.

1.5 Functional and Hemodynamic Assessment of Coronary Arteries

Cardiac imaging modalities allow for detailed morphologic analysis of the coronary vasculature. They are used as tools in clinical decision making and treatment selection of coronary artery diseases. For example, intravascular ultrasound imaging (IVUS) of a coronary

stenosis can provide information on minimum lumen area (i.e. currently a cutoff of 4 mm² is most often used) to determine severity of the disease and guide percutaneous coronary intervention (PCI).²⁸ Similarly, based on clinical guidelines, a coronary artery aneurysm of diameter >8 mm is known as a giant aneurysm, which requires anti-coagulant therapy.²⁹ Diagnostic performance of these anatomic based guidelines are improved when combined with functional and hemodynamic assessments. The following sections introduce hemodynamic indices extensively used in computational modeling and assessment of cardiovascular pathologies. Hemodynamic indices analyzed for this study are WSS, OSI, and FFR. These indices have previously been shown to have clinical significance of a disease independent or in correlation with its morphological features that may ideally lead to improved therapeutic strategies.^{28,29}

1.5.1 Wall Shear Stress

WSS is a measure of frictional force exerted on the flow surface (here arterial wall) from any flowing fluid (here blood) that can be calculated as shown below:

$$\begin{aligned}\boldsymbol{\tau}_w &= \boldsymbol{\tau} - (\boldsymbol{\tau} \cdot \mathbf{n}_w)\mathbf{n}_w \\ \boldsymbol{\tau} &= \mu (\nabla \mathbf{V} + \nabla \mathbf{V}^T)\end{aligned}\tag{1}$$

Where, $\boldsymbol{\tau}_w$ is the WSS vector, $\boldsymbol{\tau}$ is the viscous stress tensor, \mathbf{n}_w is the unit normal to the wall, μ is the blood viscosity, $(\nabla \mathbf{V})$ is the velocity gradient on the wall and $\nabla \mathbf{V}^T$ is the transpose of $\nabla \mathbf{V}$.^{30,31} It has been well established that WSS plays a role in onset and progression of atherosclerosis through the shear-dependent response of endothelial cells and activation of inflammatory cells and signaling pathways (see Figure 1.5). For example, WSS has been used as a predictive metric in the study of coronary artery bypass graft (CABG) design³², risk of thrombosis in coronary aneurysms³³, as well as coronary artery stenosis³⁴⁻³⁶ and other cardiovascular anomalies.^{27,37-40} Sankaran et al.³² computed WSS indices at different virtually created anastomosis angles of a patient with CABG and suggested angle of 70° to be hemodynamically optimal. Gutierrez et al.³³ characterized WSS

in ten Kawasaki disease patients for thrombotic risk stratification and reported a higher sensitivity compared to standard anatomic-based metrics. Chiastra et al.⁴¹ simulated coronary flow in two virtually implanted commercial stents and assessed adverse stent-induced WSS and other hemodynamic indices.

Time averaged WSS is defined as: $TAWSS = 1/T \int_0^T |\tau_w| dt$, where T is the period (here cardiac cycle). The long term biomechanical response to local hemodynamics such as vascular remodeling likely involves the integration of WSS stimuli over the cardiac cycle, which is generally represented by TAWSS.⁴²

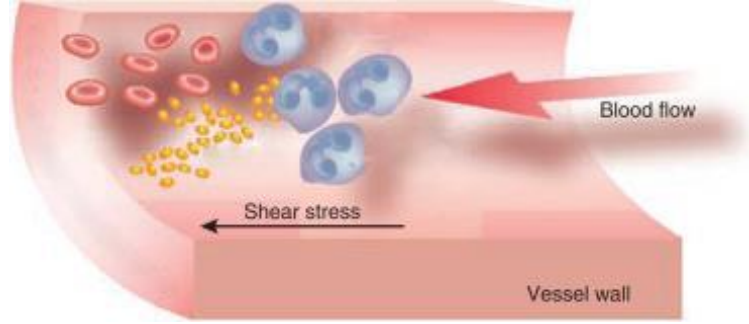


Figure 1.5 A vessel experiences wall shear stress (WSS) from flowing blood. Adverse WSS activates inflammatory cells associated with plaque formation (reproduced with permission from Li et al⁴³)

1.5.2 Oscillatory Shear Index

OSI is a measure of temporal variation in the WSS direction, defined as:

$$OSI = 0.5 \left(1 - \frac{1/T \left| \int_0^T \tau_w dt \right|}{1/T \int_0^T |\tau_w| dt} \right) = 0.5 \left(1 - \frac{|A_{pos} + A_{neg}|}{|A_{pos}| + |A_{neg}|} \right) \quad (2)$$

Where the numerator is the magnitude of the time-averaged WSS vector, and the denominator is the time-averaged value of the WSS magnitude. Figure 1.6 Figure 1.7 shows temporal variation in WSS (τ_w) where A_{pos} is the area of the positive WSS and A_{neg} is the area of the negative WSS.

When the flow is unidirectional ($A_{pos}=0$ or $A_{neg}=0$), the numerator and denominator will be equal and OSI will have the value of zero. In contrast, for bidirectional WSS throughout the cardiac cycle, area under the WSS-time curve for the positive and negative WSS will be equal ($A_{pos}=A_{neg}$), the numerator will be zero and OSI will have the maximal value of 0.5.

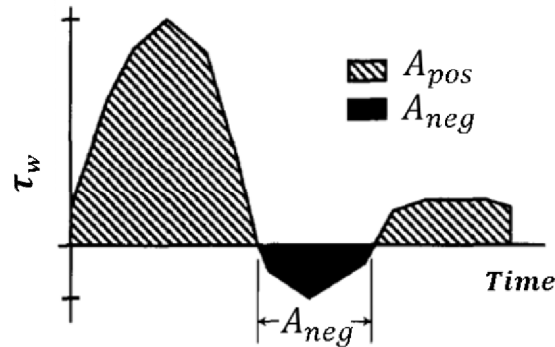


Figure 1.6 Temporal variation of WSS. Area of the positive WSS under the curve is marked by A_{pos} and area of the negative WSS under the curve is marked by A_{neg} . [Reproduced with permission from Moore et.al⁴⁴]

Overall, OSI is an indication of flow disturbance at the vessel wall and has been shown to play a role in pathogenesis of vascular diseases.⁴⁵

1.5.3 Fractional Flow Reserve

FFR has primarily been used as a diagnostic tool to identify ischemia-causing coronary artery disease (CAD) lesions and assist patient management.^{46,47} FFR is defined as a ratio of the maximum achievable myocardial blood flow in the presence of a stenosis to the hypothetical maximum flow in the absence of the stenosis under hyperemia or stress induced conditions. Since the pressure-flow relationship is linear under maximum vasodilation or maximum exercise, FFR can be approximated as the ratio of pressure distal to the stenotic lesion (P_d) to the pressure measured proximal to the lesion (here aortic pressure P_a) as shown in Figure 1.7.⁴⁸⁻⁵⁰

Recently it has been suggested that FFR measurements can be used to identify hemodynamic significance in anomalous coronary arteries. Specifically, an $\text{FFR} \leq 0.8$ (similar to CAD) has been postulated as suggestive of a hemodynamically-significant stenosis likely to cause ischemia.²⁻⁶ This modality has been introduced as an adjacent method when non-invasive imaging modalities such as computed tomography (CT) and magnetic resonance imaging (MRI) show ischemic discrepancy.^{2,6} A study by Agrawal et al. was the first to perform FFR and IVUS in a group of children with CAAs including intramural AAOCA.¹⁷ Their FFR measurements showed a decrease from baseline to the provocative testing condition and a significant improvement post-operation. All the patients with $>70\%$ intraluminal area narrowing had a hemodynamically significant FFR (≤ 0.8). In a study by Lee et al.³ on adult patients with anomalous coronary arteries, all patients that had a hemodynamically significant FFR were reported to have $>50\%$ area stenosis. In this prior study, two-year follow-up in the patients under conservative management with $\text{FFR} > 0.8$ confirmed there was no evidence of cardiac events.

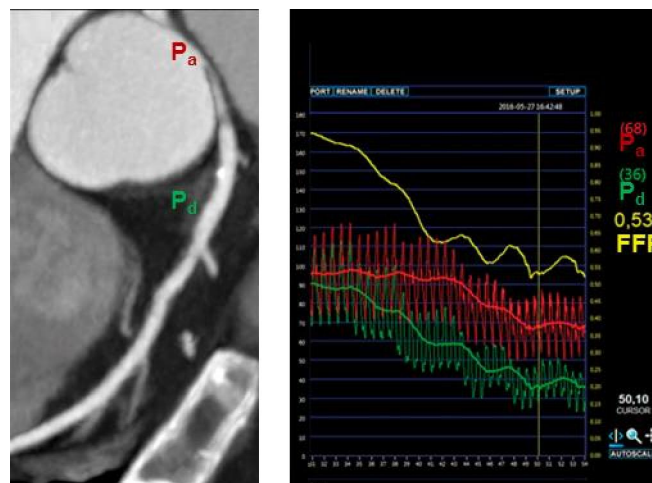


Figure 1.7 Use of FFR in clinical practice. Left: CT coronary angiogram of an AAOCA patient with proximally narrowed anomalous RCA. Right: proximal pressure waveform (red), distal pressure waveform (green) and FFR (yellow). Numbers are mean values of the waveforms.
[reproduced with permission from Zimmermann et. al ⁵¹]

Together, FFR and IVUS may also provide a comprehensive anatomical and functional assessment of AAOCA. However, the FFR method is catheter-based and invasive with higher medical costs and chances for complications. In contrast, virtually derived FFR from CT or MRI, has been introduced as a non-invasive functional assessment of CAD and shown to be a desirable tool in detecting lesion-specific ischemia.^{52,53} A meta-analysis on 5 studies that compared CT with and without FFR_{CT} to the measured FFR reported significantly improved specificity with FFR_{CT}.⁵⁴

1.5.4 Hyperemic Microvascular Resistance

Prior FFR studies only considered epicardial (proximal) contributions to the impairment of myocardial perfusion. In addition to epicardial resistance, some studies suggest that the distal microvascular alterations may also contribute to the development of myocardial ischemia.^{55,56} Such studies suggest that microcirculatory abnormalities may develop in the myocardium of the stenosed arteries. These abnormalities, explained in a form of impaired vasodilatory capacity or sustained vasoconstriction, may lead to a reduction in flow despite increasing metabolic demand under stress conditions.

Hyperemic microvascular resistance (HMR), defined as the ratio of the pressure distal to the stenosis to the distal velocity, is used to quantify this vasodilatory capacity. Van de Hoef et al.⁵⁷ evaluated stenosis severity, HMR and FFR in 225 coronary arteries. They determined low, intermediate and high HMR for the stenosed vessels based on the tertiles obtained for the reference vessel (vessel with no stenosis) and reported a vast range of FFR values across the HMR spectrum for a given stenosis severity. They showed that for a given stenosis, a low HMR may dictate a low FFR even though the resistance to flow induced by microvasculature was low at maximal vasodilation. Garcia et al.⁵⁸ proposed a mathematical relationship to formulate the observations mentioned above and indicated that epicardial stenosis, defined in terms of pressure

loss, and HMR contribute equally in FFR evaluation. These studies on the impact of HMR can be extended to the recent FFR analyses of CAAs for improved risk stratification and treatment plans.

Collectively, in the current study, we analyzed the above-mentioned hemodynamic indices to study their potential in predicting long-term morbidity (through TAWSS and OSI) and short-term ischemia (through FFR and HMR).

1.6 Patient-specific CFD Modeling

As alluded to above, patient-specific CFD simulations of the coronary arteries can play an important role in capturing realistic hemodynamic indices linked to morbidity, and may subsequently be used as a predictive tool in diagnosis and clinical treatments.⁴⁸ Replicating physiology and accurately quantifying hemodynamics requires reliable imaging and simulation modalities, appropriate material properties, proper meshing, realistic boundary conditions (BCs), and high performance computing (HPC). High resolution imaging techniques such as multi-slice CT or cardiovascular magnetic resonance (CMR) provide detailed 3D anatomic information of the model to be reconstructed. Capturing the anatomy of the coronary arteries is more challenging than other parts of the vasculature particularly due to their small size and the motion of the heart, which may introduce some modeling uncertainty. However, the available imaging techniques have been overall successful in representing patient-specific physiology.^{33,59}

Selection of accurate BCs is critical in patient-specific cardiovascular modeling. BCs represent the behavior of the vasculature downstream and upstream of the 3D model, which can significantly affect local hemodynamics. Resistance of the small arteries and arterioles of the coronary micro-vasculature affects changes in blood pressure (BP) in larger arteries and are responsible for coronary blood flow regulation. Lumped parameter network (LPN) models consider these important effects by representing them as a collection of electrical elements. When used as BCs, zero-dimensional (0D) LPN models coupled to the 3D computational domain enable

interaction of the local 3D hemodynamics with more global circulatory physiology. Parameters of the LPN models have been described in more detail in section 2.3 of the methods section.

As mentioned above, patient-specific simulations of coronary artery blood flow have been conducted using a multi-scale approach with application to acquired CAD, congenital coronary artery defects such as Kawasaki disease as well as treatment by coronary artery bypass grafting.^{32,59,60} However, this approach has not yet been applied to patient-specific models in AAOCA. The current study presents the first patient-specific image-based CFD modeling of blood flow in 6 AAOCA children to achieve the aims described below.

1.7 Aims and Hypothesis

We aim to characterize hemodynamics in AAOCA patients pre-operatively and post-unroofing by applying several advancements in patient-specific coronary artery simulations. These advancements are focused on incorporating improved coronary artery BCs that mimic the complex relationship between flow and pressure based on downstream impedance. We also aim to study the effect of high-risk anatomic features including AO and representing the lateral compression of the anomalous artery through virtual manipulation of a representative pre-operative model. The results from these aims will improve our understanding of the coronary hemodynamics in AAOCA patients and allow us to examine the postulated mechanisms involved in ischemia and morbidity.

1.7.1 Hypothesis

This study tests the hypothesis that the morphology of the anomalous coronary artery has a significant impact on local hemodynamics for patients with AAOCA. Computationally derived hemodynamic indices may predict short- and long-term pathological events such as ischemia and atherosclerosis.

1.7.2 Specific Aims

The current study has 3 specific aims:

- (1) Analyze coronary hemodynamics through patient-specific modeling of AAOCA using advanced coronary artery BCs
- (2) Assess the hemodynamic impact of the AO through virtual manipulation of a pre-operative AAOCA morphology
- (3) Characterize the effect of ostial compression through FFR assessment in the proximal anomalous coronary artery

1.7.2.1 Specific Aim 1

Analyze coronary hemodynamics through patient-specific modeling of AAOCA using advanced coronary artery BCs.

Reproducing physiologic hemodynamics requires reconstructing an accurate arterial geometry and applying BCs that are patient-specific. Previous studies in our lab included numerical simulation of the stented region of coronary arteries using a three element lumped RCR (Windkessel) model to simulate outlets downstream.⁶¹ Although conducted under several reasonable assumptions, strictly speaking the implementation of BCs in these prior simulations were not physiologic. For example, the phasic behavior of the coronary arteries was previously neglected by applying coronary inflow waveforms to computational geometries and using the simplifying RCR outlet BCs. For the current study, aortic inflow waveforms were also used, but the phasic behavior observed in the coronary arteries was modeled by implementing an intramyocardial pump along with compliance within a downstream lumped model.^{59,62,63} Other parameters of the coronary LPN including microcirculation and venous resistances have been used in several recent studies and allow us to consider the effects of regulatory mechanisms and their impact on the micro-vessel compliance.^{59,64} As part of this aim, we develop a robust protocol

for determining these parameters with specific application to AAOCA. We then analyze patient-specific coronary artery hemodynamics pre-operatively and post-unroofing.

1.7.2.2 Specific Aim 2

Assess the hemodynamic impact of the AO through virtual manipulation of pre-operative AAOCA morphology

The exact mechanism of ischemia in AAOCA patients is unclear. One of the mechanisms hypothesized is that the abnormal AO limits coronary artery flow reserve and/or introduces adverse flow patterns and WSS alterations previously linked to the onset and progression of atherosclerosis.²⁴⁻²⁶ With this aim, we parametrically assess the impact of AO on coronary artery flow patterns and related hemodynamic indices. Models for this analysis are obtained by virtually revising a representative pre-operative model through computer-aided design and image processing software packages to create a range of AO that covers both acute and non-acute angles of the origin, and is aligned with values seen clinically.⁶⁵ Resultant WSS and OSI on the inner and outer walls of the proximal anomalous coronary arteries of the original and rotated models are then compared statistically.

1.7.2.3 Specific Aim 3

Characterize the effect of ostial compression through FFR assessment in the proximal anomalous coronary artery

An ostial stenosis accompanied by compression of the anomalous artery during exertion can increase the risk of ischemia. It has been recently suggested the use of FFR can be extended to identify ischemia in anomalous coronary arteries.² We aim to mimic the lateral compression of a representative pre-operative model by generating elliptical cross-sections along the proximal coronary tract with varying severity of luminal area reduction (i.e. stenoses). The range of

stenosis severities observed in clinical reports were 50-70%.^{3,5,17} We selected 60%, 65% and 70% area stenosis, which were identified near the hemodynamic limit identified for anomalous coronary arteries by clinical measurements of Agrawal et al.¹⁷ Simulation results are used to compute virtual FFR (vFFR) values for the original and constricted models. In addition to assessing different stenosis severities, microvascular resistance under hyperemic or stress-induced conditions and its effect on FFR are determined to include the contribution of the downstream micro-vasculature resistance in addition to the epicardial stenosis resistance and to characterize the anatomy with clinical significance. Results from this aim will provide non-invasive delineation of coronary flow changes and prediction of ischemia that may ultimately lead to risk stratification of AAOCA patients and assist in clinical decision making.

2 MATERIALS and METHODS

2.1 Overview

This chapter explains the basic steps used in computational modeling of AAOCA patients and includes reconstructing the geometry from MRI data, assigning patient-specific BCs, generating the mesh, solving the governing equations by means of a numerical solver, assessing mesh independence and post-processing hemodynamic results to analyze statistical significance (Sections 2.2-6). A summary of the steps conducted for patient-specific modeling of AACOA in the current study is indicated in Figure 2.1. Sections 2.7-9 are related to specific aims 1, 2, and 3, respectively, and discuss the methods to measure anatomical features and to create virtually rotated as well as compressed coronary arteries.

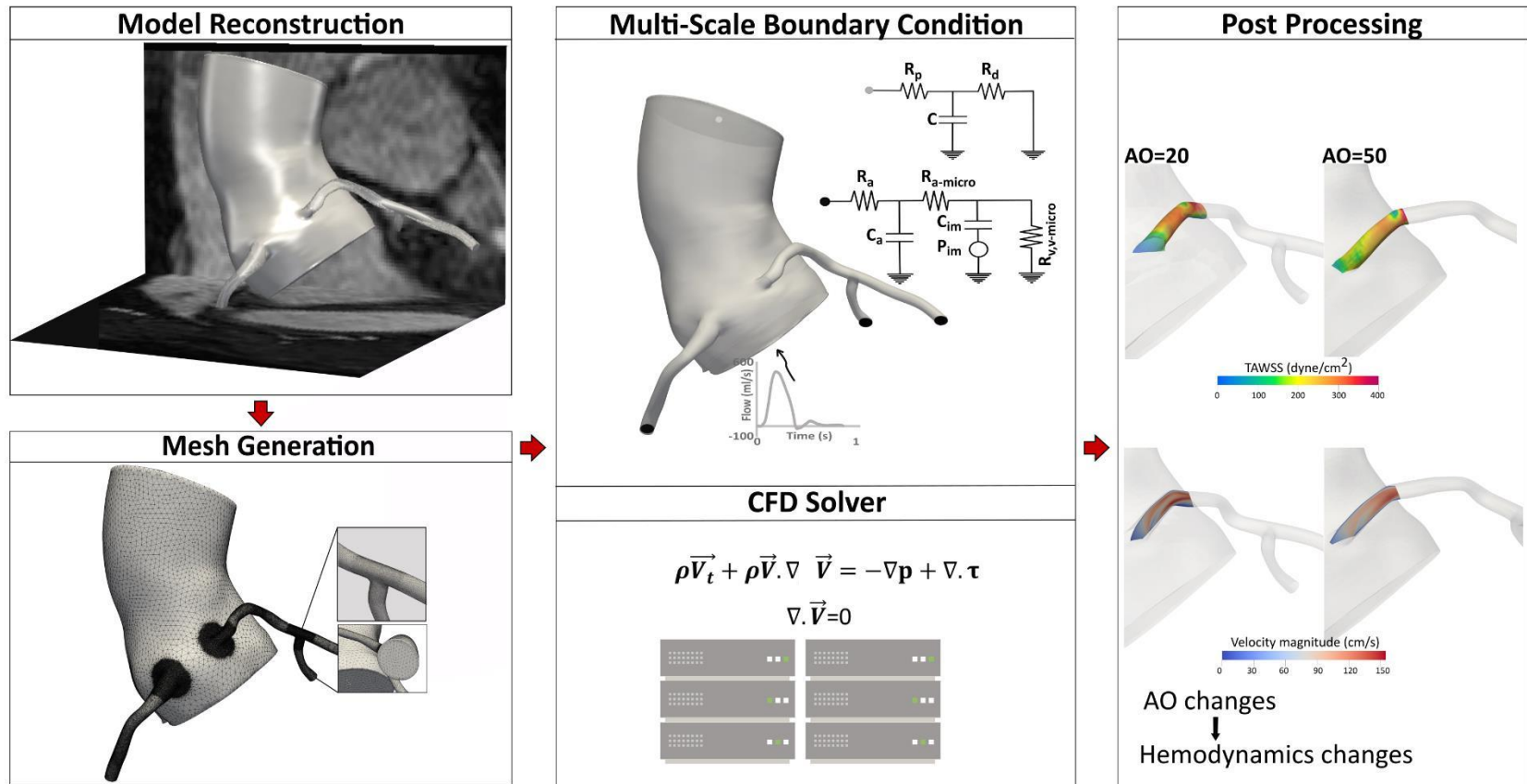


Figure 2.1 A summary of the steps conducted for patient-specific modeling of AACOA in the current investigation included model reconstruction, mesh generation, assigning multiscale BCs, solving the governing equations using a CFD solver, and post-processing and visualizing hemodynamic changes including pressure, velocity and indices of WSS. All terms have been introduced in SYMBOLS.

2.2 Geometry Reconstruction of AAOCA Patients from MRI Data

Following IRB approval, clinically indicated CMR of 6 intramural AAOCA patients (median 13.5 years, range 9-17 years), was performed at Children's Hospital of Wisconsin. Coronary imaging was performed with a vector electrocardiogram (ECG) and respiratory navigator-gated, fat-suppressed 3D steady state free precession (SSFP) sequence covering the coronary artery origins and course. Its parameters are as follows - Repetition time (TR)/Echo time (TE) = 373.3/1.6 milliseconds, flip angle = 90° , field of view = 384×512 mm, matrix = 256×256 , slice thickness = 0.8 mm, and voxel size = $1.4 \times 1.4 \times 0.7$ mm³. Two patients had CMR pre-operatively and post-unroofing, and 4 patients had CMR only post-unroofing. Three patients had anomalous left and three patients had anomalous right coronary arteries. MRI scans of the patients were de-identified and series numbers for use with computational modeling were provided by clinical colleagues. The images were then loaded into SimVascular (simtk.org). Centerlines for the ascending aorta, LMCA and RCA as well as LAD and LCX were created through points positioned within each of these arteries. Artery contours were created through manual segmentation. SimVascular was then used to conduct a series of Boolean operations to join the arteries and blending was performed to create smooth transitions between them using each patient's imaging data as a visual guide (see Figure 2.2). Finally, the resulting 3D models were shared with collaborating clinicians in order to ensure they were a geometrically representative 3D model of the blood flow domain and morphological corrections were implemented as needed in response to clinical suggestions.

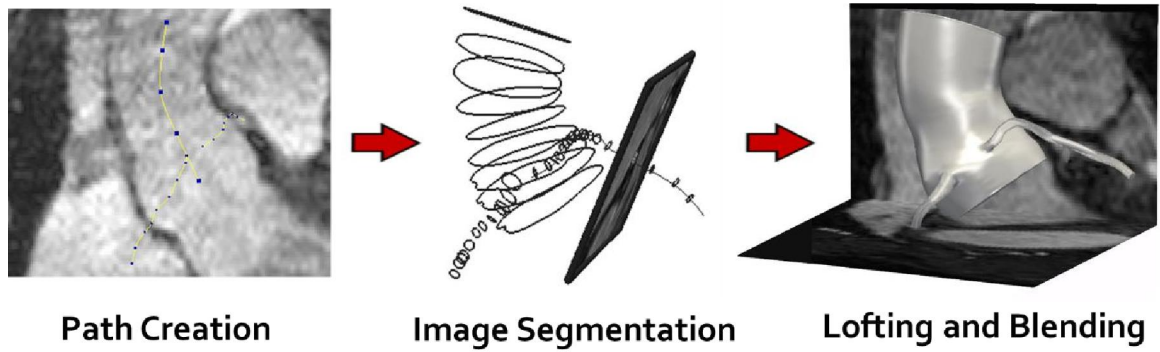


Figure 2.2 Steps of the CMR image-based model reconstruction process. Centerline path lines are created, 2D segments are generated manually and lofted to reconstruct the 3D geometry.

2.3 Boundary Conditions

An open loop heart model was used in this study for specifying BCs. Aortic flow was assigned at the inlet and a coupled multiscale method was used to describe the effect of the arterial tree downstream of the outlets that is not present in the 3D computational model domain.^{59,66–68} This effect, as mentioned in section 1.6, was included by representing the vasculature as 0D LPN models analogous to the electrical circuits. Parameters of the LPN model were determined to replicate dominant coronary flow in diastole. A schematic showing the general assignment of these BCs is provided in Figure 2.1. The following details explain how parameters for inlet and outlet BCs are selected in a patient-specific manner under resting (Aims 1 & 2) and stress-induced (Aim3) conditions.

2.3.1 Inflow and Left Ventricular Pressure

Aortic inlet flow is obtained either from the clinical phase contrast MRI (PC-MRI) measurements, if available for a particular patient, or by customizing a normalized waveform obtained from the literature.^{66,69} When PC-MRI data were available, the stack of magnitude and phase image pairs were loaded into Segment (MEDVISO, Lund, Sweden) for quantification and waveform creation. Briefly, segmentations at each time point were created using the manual region of interest (ROI) tool for each image pair (i.e. magnitude and phase). An eddy current compensation algorithm to reduce background phase error was then applied and a flow waveform was extracted as the program applies segmentations to each portion of the cardiac cycle. In other patients, the aortic flow rate, but not necessarily a waveform under resting and stress-induced (i.e. Dobutamine) conditions was obtained by our clinical colleagues. In these cases, a normalized aortic flow waveform was made patient-specific using the measured patient cardiac output (CO) and heart rate.^{66,69}

The left ventricular pressure (LVP) data was not available for patients as it considered to be an invasive measurement, particularly for children and young adults. In this study, LVP waveforms were obtained using a normalized LVP available in the literature.⁷⁰ The waveform was made patient-specific using each patient's measured systolic BP (SBP) during resting or stress-induced Dobutamine conditions and assuming a normal end diastolic ventricular pressure of 6 mmHg.⁷¹ Flow and pressure waveforms were then aligned consistent with their temporal relationship from the Wigger's diagram⁷² using a MATLAB program developed in our laboratory.

2.3.2 Outlet Boundary Conditions

LPN outlet BCs include 3 element (i.e. RCR) Windkessel model at the aortic and 6 element models at the coronary outlets (see Figure 2.1). To obtain individual parameters of each LPN circuit, it was required to determine total vascular resistance (R_{tot}), total coronary resistance ($R_{cor,tot}$), aortic and coronary outlet resistances (R_{aorta} , $R_{cor,i}$), total coronary compliance ($C_{tot(left,right)}$), and outlet compliance (C , $C_{cor,i}$) in a sequential manner. Resistance and compliance values of each outlet were then distributed using appropriate ratios to yield individual resistance and compliance parameters.

Total vascular resistance for each patient was initially calculated as the ratio of the patients' CO and mean BP (MBP) as shown by Equations. 3-4. SBP and DBP are systolic and diastolic BP.

$$MBP = \frac{1}{3}SBP + \frac{2}{3}DBP \quad (3)$$

$$R_{tot} = \frac{MBP}{CO} \quad (4)$$

2.3.2.1 Aortic Outlet BCs

Assuming that coronary flow represents 4% of the CO⁷³, 96% of the flow goes to the aortic outlet and resistance at this outlet can be calculated as ($R_{aorta} = \frac{R_{tot}}{0.96}$). The aortic (systemic) outlet model as described by a 3 element (RCR) circuit (Windkessel model is shown in Figure 2.3). Resistance of the aorta was composed of proximal (R_p) and distal (R_d) resistance in series. The ratios of R_p and R_d to the total aortic resistance (R_{aorta}) were tuned in accordance with prior studies indicating that the majority of the systemic resistance is in distal vessels.³² Arterial compliance is denoted by (C) and was tuned to match the measured pulse pressure of each patient during resting or stress-induced Dobutamine conditions using the pulse pressure method.⁷⁴

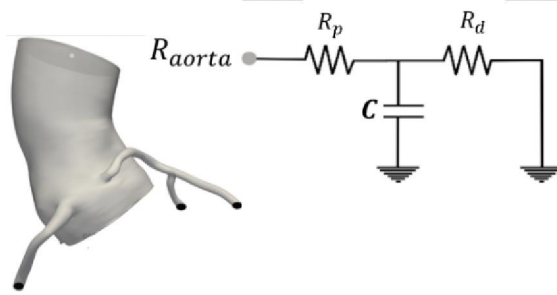


Figure 2.3 A LPN 3-element Windkessel model (R_p , C , R_d) is used at the aortic outlet to describe the behavior of the systemic circulation

2.3.2.2 Coronary Outlets BCs

2.3.2.2.1 Resistance Parameters

Total coronary resistance was calculated as ($R_{cor,tot} = \frac{R_{tot}}{0.04}$). The resistance of each coronary outlet ($R_{cor,i}$) was obtained based on generalized Murray's law that relates resistance and area of each outlet to the total coronary resistance and area as depicted by Equation 5.⁷⁵

$$R_{cor,i} = \frac{\sum_{j=1}^n \sqrt{A_i}^{2.6}}{\sqrt{A_i}^{2.6}} R_{cor,tot} \quad (5)$$

Coronary artery models for each outlet include coronary arterial resistance (R_a), coronary arterial compliance (C_a), coronary arterial microcirculation resistance ($R_{a-micro}$), coronary intramyocardial compliance (C_{im}), coronary venous and venous microcirculation resistance ($R_v + R_{v-micro}$), and intramyocardial pressure (P_{im}). (Figure 2.4)

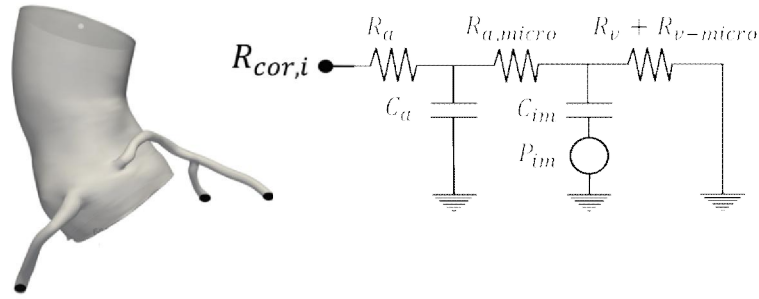


Figure 2.4 A coronary artery LPN model is used at each outlet to describe the behavior of the coronary circulation. It includes 3 resistance and 2 compliance elements as well as the intramyocardial pressure to account for the phasic behavior between coronary artery flow and pressure.

Arterial, arterial microcirculation, venous microcirculation and venous resistance were obtained at each outlet using the ratios given by Equation. 6.

$$R_a = 0.32 R_{cor,i} \quad R_{a,micro} = 0.52 R_{cor,i} \quad R_v + R_{v-micro} = 0.16 R_{cor,i} \quad (6)$$

These ratios under resting conditions were estimated from the pressure drop over the coronary vasculature.⁷⁶ Under Dobutamine stress conditions, CO and coronary artery blood flow increase as a result of secondary vasodilation caused by an increase in myocardial demand.⁷⁷ Using the data reported by Stephens et al and Beanlands et al^{78,79}, coronary artery blood flow as the percentage of CO was calculated and reported to be 4% , the same value used for the resting condition. This is in agreement with the data from Astrand⁷³, who reported that coronary artery blood flow was maintained at 4% of the CO under exercise conditions and also confirmed that the

effect of exercise and Dobutamine-induced stress conditions on myocardial perfusion are similar.^{77,80} Resistance ratios under stress conditions need to be modified because of the altered behavior of the downstream vasculature. While vasodilation occurs mostly at the micro-vessels, smaller arteries become vasoconstricted. This leads to a higher contribution for arterial resistance and lower contribution of the arterial microcirculation resistance. This behavior has been explained by Chilian et al.^{81,82}, under dipyridamole and norepinephrine infusion as shown in Figure 2.5.

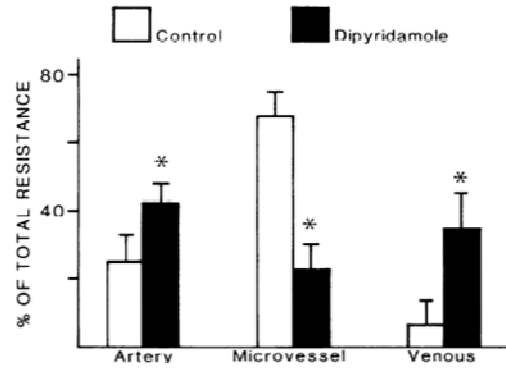









Figure 2.5 . Relative distribution of coronary artery resistance in 3 vascular compartments during control conditions and dipyridamole infusion. Adapted with permission from Chilian et al.⁸¹

However, as mentioned above, since Dobutamine produces hemodynamic changes similar to exercise⁸⁰, we use exercise-induced coronary redistribution values reported by Kim et al⁵⁹, denoted by Equation. 7.

$$R_a = 0.64 R_{cor,i} \quad R_{a,micro} = 0.2 R_{cor,i} \quad R_v + R_{v-micro} = 0.16 R_{cor,i} \quad (7)$$

Table 1 summarizes the steps for calculating LPN resistance parameters using the available clinical measurements and literature derived inputs summarized above.

Table 1 Determination of the resistance parameters for the aortic and coronary outlet LPN models

Model inputs		Determination					
Clinical	Systolic BP		Mean BP (Eq. 3)				
	Diastolic BP						
	Cardiac output (CO)		Total vascular resistance (R_{tot} , Eq. 4)				
Literature derived	Aortic flow (96% of the CO) ⁷³			Aortic outlet resistance ($R_{aorta} = \frac{R_{tot}}{0.96}$)			
	Contribution factors of the downstream resistance of the aortic outlet ³²					R_p, R_d	
	Total coronary flow (4% of the CO) ⁷³			Total coronary resistance ($R_{cor,tot}$)			
	Murray's law (Distributing the flow or resistance proportional to the outlet areas) ⁷⁵					Resistance at each coronary outlet ($R_{cor,i}$, Eq. 5)	
	Pressure distribution over the coronary vasculature to determine contribution factors of the downstream resistance at each coronary outlet ⁷⁶						$R_d, R_{a,micro}, R_v$ (Eq. 6 & 7)

2.3.2.2.2 Compliance Parameters

Initial estimation for the total left and right coronary compliance were adapted from the prior studies.^{59,83} Compliance at each outlet is proportional to its cross-sectional area and obtained using Equation 8.

$$C_{cor,i} = \frac{A_i}{\sum_{j=1}^n A_j} C_{tot(left/right)} \quad (8)$$

Intramyocardial and proximal compliance were obtained from the compliance of each coronary outlet ($C_{cor,i}$) using Equation 9. The ratio was previously suggested by Kim et al.⁵⁹, and is in agreement with the data reported by the literature for the compliances of coronary microcirculation and small coronary arteries.^{68,84}

$$C_a = 0.11 C_{cor,i} \quad C_{im} = 0.89 C_{cor,i} \quad (9)$$

Compliance values were tuned over multiple simulations so that a physiologic coronary artery waveform matching aimed pressure and flow distributions was obtained. Under Dobutamine stress conditions, arterial pressure increases.⁸⁵ α -vasoconstriction stimulation will reduce the compliance of the intramyocardial vessels improving the retrograde to antegrade flow oscillations of the endocardial layers.^{86,87} It also has been shown that compliance of the proximal epicardial and intramyocardial vessels decreases with increasing pressure.^{88,89} Figure 2.6 indicates the relationship between area cross-sectional compliance and diastolic pressure by Chilian et al.⁶⁶

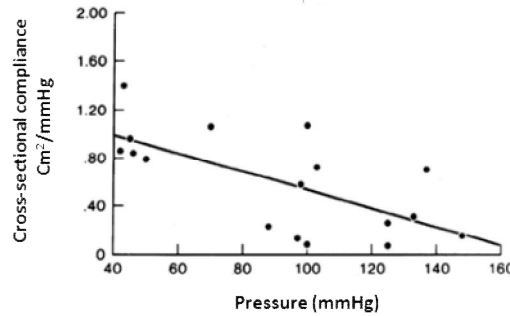


Figure 2.6 Relationship between coronary proximal compliance and pressure, adapted with permission from Chilian et al.⁸⁸

We estimated the gradient of the compliance using the slope of the lines from these data to calculate the epicardial and intramyocardial compliance under stress conditions ($C_{a,stress}$ and $C_{im,stress}$) using equations 10 and 11:

$$C_{a,stress} = C_{a,rest} + m * (P_{stress} - P_{rest}) \quad (10)$$

$$C_{im,stress} = C_{im,rest} + m * (P_{stress} - P_{rest}) \quad (11)$$

Where P_{rest} and P_{stress} are the mean BP under resting and stress conditions, $C_{a,rest}$ and $C_{im,rest}$ are the compliance values under resting conditions.

Table 2 summarizes the steps for calculating LPN compliance parameters using the available clinical measurements and literature derived inputs.

2.3.2.2.3 Pressure Parameters

Intramyocardial pressure in the left and right coronaries was computed from the LVP using Equation 12.

$$P_{im,left} = 1.5 LVP \quad P_{im,right} = 0.5 LVP \quad (12)$$

Experimental measurements confirm that the left intramyocardial pressure is higher than the LVP suggesting an average split ratio value around 1.6, which was in good agreement with the ratio recommended by SimVascular documentation, and hence used in our simulations.⁹⁰⁻⁹³ Since the right ventricle operates at a lower pressure, we would expect to see a lower intramyocardial pressure exerted on the right coronary artery compared to the left coronary artery.⁹⁴

Table 3 summarizes the steps for calculating P_{im} using the available clinical measurements and literature derived inputs.

Table 2 Determination of the compliance parameters of the LPN models for the aortic and coronary outlets







Model inputs		Determination			
Clinical	Systolic BP		Compliance (C) is tuned according to the pulse pressure method until measured systolic and diastolic BPs are achieved.		
	Diastolic BP				
	Initial estimate for the aortic compliance (C)				
Literature derived	Initial estimate for the total left and right coronary compliance ($C_{total,left}$ & $C_{total,right}$)		Compliance at each coronary outlet ($C_{cor,i}$, Eq. 8)		
	Contribution factors for the arterial and intramyocardial compliance			C_a, C_{im} (Eq. 9, 10 & 11)	Compliance values are adjusted until the systolic to diastolic peak flow ratio is physiological.

Table 3 Determination of the intramyocardial pressure for the coronary artery LPN model outlets

Model inputs		Determination				
Clinical	Systolic BP		Patient-specific LVP waveform is obtained through scaling a normalized waveform with the patient's systolic BP.			
	LVP waveform					
Literature derived	Contribution factor for the left intramyocardial pressure.			$P_{im} (left) = 1.5 LVP$		
	Ratio of the right to left ventricular pressure ($RVP \sim 1/\{3 - 4\}LVP$). ⁹⁴				$P_{im} (right) = 0.5 LVP$	

Under Dobutamine-induced stress conditions, contractility will increase as a result of both α and β adrenergic stimulation.^{95,96} Data reported by Bovendeerd et al.⁹⁷ indicates that at different contractility levels, the ratio of intramyocardial to the left ventricular pressure is maintained. This prior finding suggests that under Dobutamine stress conditions, Equation 12 is still relevant. This is also in agreement with Mihailescu et al.⁹⁸, where the intramyocardial to LVP ratio did not change at different perfusion pressures (50-100 mmHg).

Table 4 lists data that were used as clinical inputs for determining BC parameters and includes heart rate (HR), cardiac cycle (T), BP (systolic BP/diastolic BP) and CO. Final parameters of the Windkessel and coronary artery outlets based on these inputs and the methods described are displayed in Table 5.

Table 4 Patients' clinical measurements

Patient		HR	T (s)	SBP (mmHg)/DBP (mmHg)	CO (L/min)
1	PRE	82	0.73	102/70	6.00
	POST	64	0.94	123/64	5.60
2	PRE	77	0.78	130/60	6.00
	POST	68	0.88	120/78	5.50
3	POST	82	0.73	117/66	9.00
4	POST	57	0.95	109/50	4.00
5	POST	60	1.00	127/55	5.10
6	POST	105	0.57	118/60	7.50

Table 5. Parameter values of the LPN models to describe downstream of the coronary artery and aortic outlets at rest (Units: Resistance = 10^3 dyne/cm⁵ and Compliance= 10^{-5} cm⁵/dyne)

Coronary Artery Parameters								Aortic Windkessel Parameters		
Patient		Outlet	R _a	R _{a micro}	R _v	C _a	C _{im}	R _p	C	R _d
1	PRE	RCA	16.8	27.3	8.40	0.28	2.23	0.05	170	0.92
		LCX	21.2	34.4	10.6	0.41	3.30			
		LAD	23.1	37.5	11.5	0.39	3.11			
	POST	RCA	29.3	47.6	14.7	0.28	2.23	0.06	94.5	0.99
		LCX	21.4	34.8	10.7	0.19	1.56			
		LAD	20.1	32.7	10.1	0.20	1.64			
2	PRE	RCA	35.2	57.2	17.6	0.28	0.28	0.07	52.0	1.24
		LCX	29.6	48.0	14.8	0.19	1.55			
		LAD	27.4	44.5	13.7	0.20	1.65			
	POST	RCA	42.8	69.5	21.4	0.28	2.23	0.08	110	1.32
		LCX	21.2	34.5	10.6	0.14	1.11			
		LAD	43.8	71.2	21.9	0.26	2.09			
3	POST	RCA	18.3	29.8	9.20	0.28	2.27	0.04	94.0	0.77
		LCX	28.6	46.5	14.3	0.14	1.13			
		LAD	12.4	20.1	6.20	0.26	2.10			
4	POST	RCA	51.6	83.8	25.8	0.28	2.27	0.08	61.0	1.46
		LCX	41.9	68.2	20.9	0.16	1.27			
		LAD	24.2	39.4	12.1	0.24	1.94			
5	POST	RCA	15.3	24.9	7.67	0.28	2.27	0.05	60.0	0.94
		LCX	40.0	65.1	20.0	0.16	1.31			
		LAD	24.6	39.9	12.3	0.24	1.94			
6	POST	RCA	24.7	40.2	12.4	0.28	2.23	0.06	70.0	1.03
		LCX	47.0	76.4	23.5	0.12	0.97			
		LAD	15.9	25.8	7.94	0.28	2.23			

2.4 Meshing

After BCs were defined, geometries were meshed for use in performing CFD simulations. Since our geometries include multi-scale dimensions (i.e. the size of the aorta is about one order of magnitude larger than the size of the coronary artery), mesh elements were defined proportional to the size of the arteries using the "local mesh" option in SimVascular. Regional mesh refinement was also performed to generate more elements for locations with high velocity gradients and expected flow disruptions. Applying this locally selective mesh refinement allows us to create a mesh with smooth transitions from the small coronary arteries to the larger aortic area while also considering computational time and resources. (See Figure 2.1, mesh generation)

The initial mesh for each patient and case was generated by using the maximum edge size suggested within SimVascular. Although the flow remains laminar based on the Reynolds number calculation under both resting and stress conditions imposed for the current work, a well-resolved mesh that is able to capture the high velocity gradients created near the wall elements of the luminal surfaces play a critical role in the calculation of WSS indices. Boundary layer meshing was therefore initiated with its thickness (δ) designed to capture approximately 93% of the average velocity outside the boundary. Although this approach is around 6% less than the 99% criteria for the boundary layer thickness ($\delta_{99\%}$), it provides improved resolution of velocity inside the boundary layer as elements are spread over a lower range of velocities. This approach is also in agreement with Fernholz⁹⁹, which introduces boundary layer displacement as a fluid mechanically interpretable measure of the thickness of the boundary layer and is about 1/3 of the $\delta_{99\%}$.

A mesh independence study was performed with the above details in mind to ensure that the resulting indices, specifically TAWSS, were independent of the mesh size. To select the best model for studying mesh independence, shear rate was estimated for the three coronary artery outlets of each patient, which was found to be most pronounced for patient 1. (see Table 6) The

acute AO and curvatures induced by the intramural section also made flow patterns from patient 1 more susceptible to disruption along with associated velocity and WSS gradients.

Table 6 Shear rate based on average velocity at the coronary outlets of the patients

Patient		shear rate (1/s)		
		LAD	LCX	RCA
1	PRE	1922	1222	739.1
	POST	1155	1081	1067
2	PRE	933.1	944.1	969.7
	POST	967.0	836.9	937.8
3	POST	1527	1195	766.3
4	POST	660.8	1010	705.2
5	POST	1156	1243	1076
6	POST	1572	1155	649.1

Mesh refinement was performed by decreasing the maximum edge size with 0.01 cm, 0.005 cm and 0.002 cm increments. Boundary layer thickness (δ) is defined as the portion of the maximum edge size in the software. Hence a higher portion is necessary for a smaller maximum edge size to capture the same boundary layer thickness. Portion of the edge size was increased based on the explanation above with each refinement. If the software was not able to create the mesh, the portion was reduced in 0.02 cm increments until the mesh was successfully created. Figure 2.7 shows the radial velocity profile from a cross-section located at the distal LMCA for nine different mesh sizes from 340K to 9M elements. Velocity profiles are similar for mesh sizes >3M.

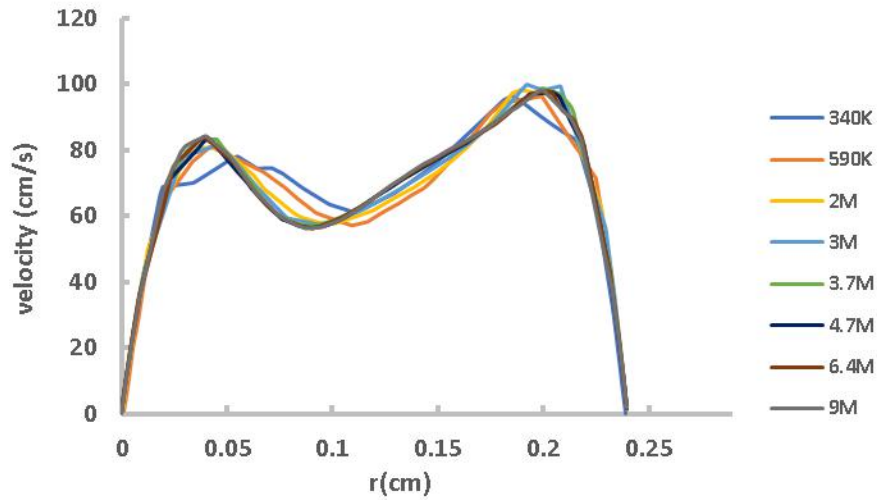


Figure 2.7 Velocity profile in a cross-section of the distal LMCA for different mesh densities. Velocity profiles are similar for mesh sizes $>3M$.

We continued to report TAWSS for bands along the LMCA as well as its LAD and LCX branches. The data shown in Figure 2.8 compares TAWSS values averaged over the bands for nine different mesh sizes. The distance of the bands is from the bifurcation and diameter multiples of the artery. As can be observed from the figure, the difference between the TAWSS values decreases with increasing mesh size. A mesh of 3.7M elements showed a percentage error $<3\%$ relative to the successive mesh, and was therefore determined to be suitable for simulations in the current work.¹⁰⁰ The maximum edge size used for 3.7M elements was 0.019 cm. We also compared the results for 2, 3 and 4 boundary layers. The difference in TAWSS between 3 and 4 boundary layers was $<3\%$ and the mesh with 3 boundary layers was selected for simulations moving forward.

For models created from other patients with more modest coronary artery angulation, mesh parameters were set by: 1) determining the average velocity of LMCA, 2) calculating 93% of this average velocity for consistency with the analysis mentioned above, 3) setting boundary layer thickness from 93% of the velocity, 4) starting with the edge size used in creating the 3.7M

elements for the patient featured in our mesh analysis, 5) calculating the portion of the edge size from the boundary layer thickness and the edge size and 6) iterating as discussed.

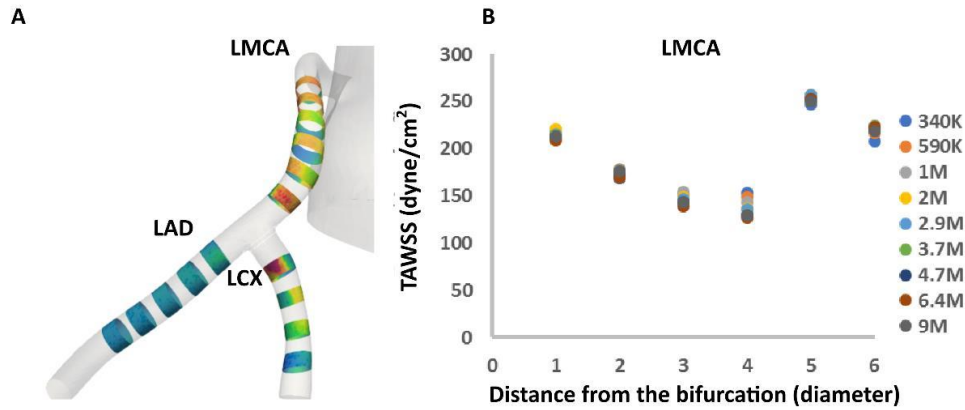


Figure 2.8 Mesh analysis for TAWSS. (A) Image of the LMCA, LAD and LCX with bands along these arteries at diameter multiples distal to the bifurcation. (B) TAWSS values for nine mesh sizes along the LMCA.

2.5 Computational Setup

Governing equations including conservation of mass (continuity) and momentum (incompressible Navier-Stokes) were solved using a stabilized finite element method in SimVascular.¹⁰¹ Walls were assumed to be rigid and blood was treated as a Newtonian fluid with a viscosity of 4 cP and density of 1.06 g/cm³. The Newtonian assumption was justified as the estimated shear rate in the coronary arteries was $>100 \text{ s}^{-1}$ for these patients.¹⁰² Residual errors of $< 1 \times 10^{-3}$ were achieved for all simulations with maximum number of 10 non-linear iterations for each time step. Simulations were run for 6-10 cardiac cycles until BP fields and flow rates at the inlet and outlets did not change more than 1% from the previous cycle.⁶⁰ The simulation time step size was selected such that Courant–Friedrichs–Lewy (CFL) number was < 1 . Data files for the simulation were created and submitted to 48-96 cores of the cloud-based HPC resources of the SimVascular Gateway that is part of the XSEDE architecture. Simulation results were then saved for twenty time points per

cardiac cycle as "vtu" and "vtp" formats, which include the data of the solid mesh and the exterior elements of the mesh. Data from the last cycle of each simulation was used for visualization and analysis.

2.6 Hemodynamics Visualization, Quantification and Statistical Analysis

Simulation results for blood flow velocity, BP, TAWSS and OSI were visualized and quantified using SimVascular and Paraview (Kitware, Inc, Clifton Park, NY, USA). To perform detailed local quantification, TAWSS and OSI were averaged within regions located on the inner and outer walls of the LMCA and RCA at fixed intervals (i.e. diameter multiples distal to the ostium). The length and diameter of the coronary arteries were different between all patients due to factors such as body surface area. Biomechanical homeostasis suggests WSS stimuli should be similar when normalizing for such differences.¹⁰³ Therefore, it is common to express results using more generalizable indices such as length as a function of diameter (here diameter multiples from the ostium). This provides a potentially more consistent comparison between the models of each patient during the pre and post-unroofing states. In all, >250 segments were analyzed for data analyses of Aims 1 and 2. vFFR values were also computed for the original simulation and those with proximal stenoses at low, intermediate and high HMR for Aim 3.

Data are expressed as mean \pm SD. Student's t-test, which has been deemed appropriate for small sample size (i.e. sample size <5),¹⁰⁴ was performed to compare TAWSS and OSI between the groups of patients pre-operatively and post-unroofing, as well as the right vs left coronary arteries as compared to contralateral normally-arising vs unroofed arteries. ANOVA with post-hoc Tukey test was used to determine the TAWSS and OSI difference between different AOs of the representative and rotated models. A *P*-value <0.05 was considered significant.

2.7 Measurement of the Length of Intramurality, Eccentricity Index and AO

Morphological parameters associated with ischemia including intramurality, eccentricity and AO were quantified in this study. These parameters have been known as morphologic (i.e. anatomic) indices for AAOCA risk stratification.¹⁰⁵ Length of intramurality was calculated by subtracting the length of LMCA centerline created during model creation in SimVascular before and after unroofing. Eccentricity index was defined as the ratio of the ostial area to area of the circle with a diameter equal to the length of the straight-line connecting points of the major chord on the ostium (Figure 2.9). This index is equal to 1 for a circular ostium and <1 for an elliptical ostium.¹⁰⁶ Length of intramurality and eccentricity index were compared pre-operatively and post-unroofing.

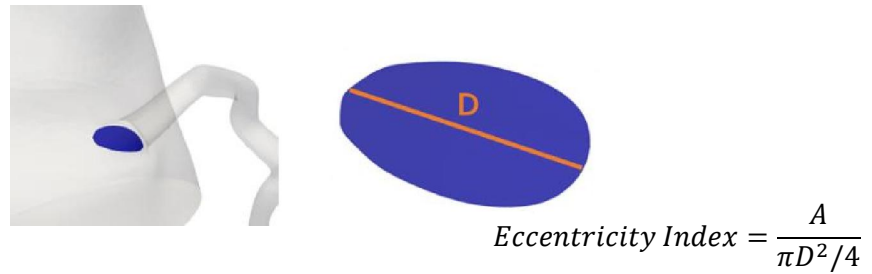


Figure 2.9 Approach to calculate eccentricity index from the area of the ostial surface (A) using the length of the line connecting points of the major chord

Two approaches were used by prior studies to calculate AO. In the first method, AO was calculated from the 3D angle between the normal to the ostial surface and proximal coronary artery.¹⁰⁶ The second approach is based on the methods applied using user-selected 2D imaging planes.¹⁰⁷

The 3D method was used in this study and may be more repeatable since it is believed to have less user bias than what is inherent in the selection of planes required for the 2D approach. Briefly, surface meshes from the model were imported into VMTK (www.vmtk.org) and the

centerlines were determined. The centerline file and mesh were then imported into Paraview. As depicted in Figure 2.10(A), a plane tangent to the ostium was created and its normal vector was obtained. Another vector was defined with the starting point at the center of the ostium and the end point selected on the centerline on the proximal length of the artery near to the ostium. AO was then extracted as the inverse sine of these two vectors.

In the 2D approach, a plane parallel to the aortic annulus was intersected with the coronary artery ostium and AO was obtained as the angle between the line along the wall of the coronary artery sinus and the line along the proximal course of the coronary artery (Figure 2.10(B)).

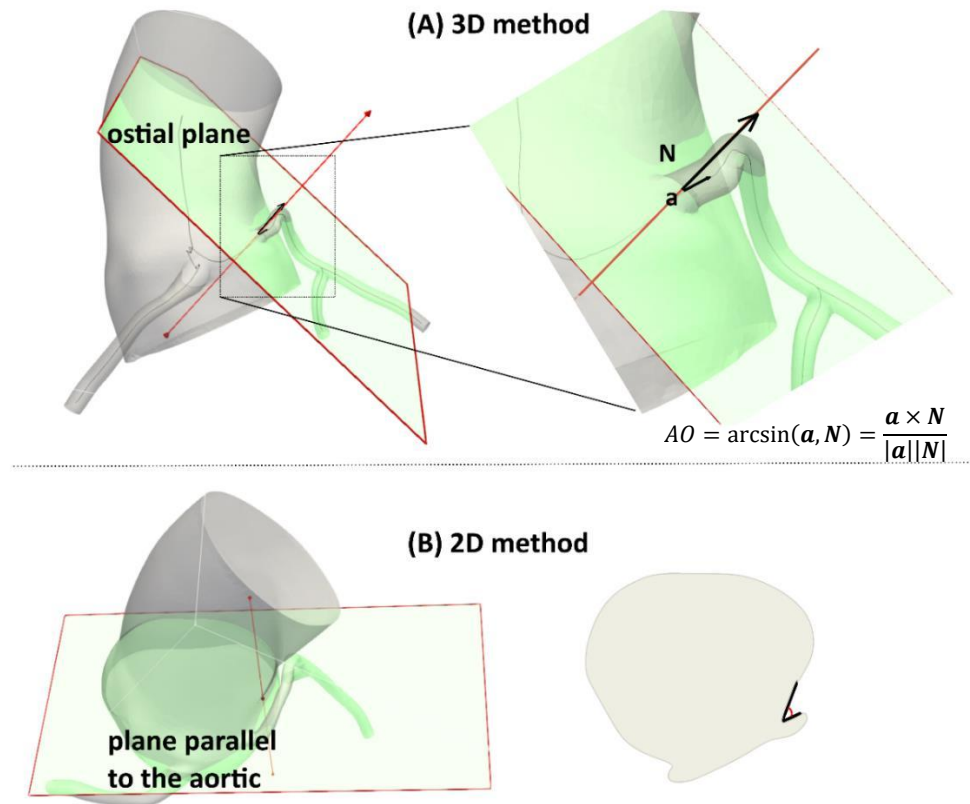


Figure 2.10 Approaches to calculate AO (A) using a prior 3D method from the vector normal to the ostium plane and the vector tangent to the proximal artery, as compared to a prior method (B) from 2D images selecting planes.

2.8 Virtual Alteration of the Angle of the Origin

As mentioned in the specific aims, by rotation of the anomalous coronary artery, various AO severities can be characterized. The angles selected for analysis were the patient's given AO as well as 20, 35 and 50 degrees. This includes both acute and non-acute states of the AO as presented by Cheezum et al.¹⁵, and is compatible with a prior study by Formato et al.¹⁹ where the AOs were specified as 20, 35 and 50 degrees. A representative pre-operative model originally reconstructed from SimVascular was saved as a Parasolid file and loaded into SolidWorks (Dassault Systèmes, Vélizy-Villacoublay, France). A plane was defined at the center of ostium orthogonal to the aortic surface. The abnormally arising coronary artery was then rotated around the normal vector of the plane and intersected with the aorta to create the new ostium and to achieve the desired AO. Figure 2.11 provides an illustration of the original and range of virtually rotated models.

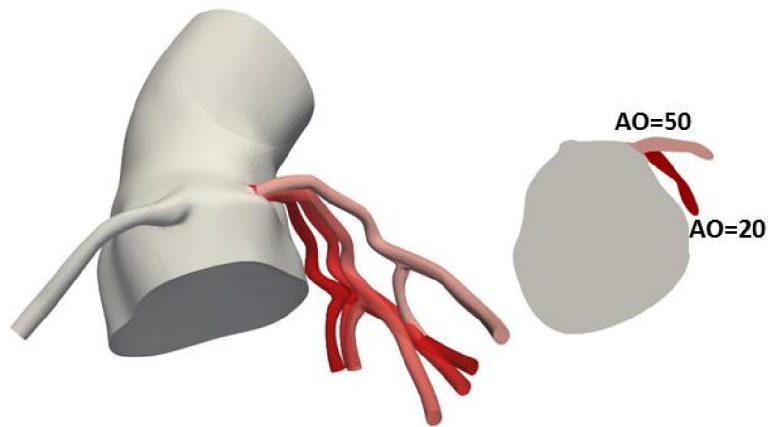


Figure 2.11 Virtual rotation of the anomalous LMCA. Left: 3D view of a representative pre-operative model with $AO = 30^\circ$ along with virtually rotated AOs of 20, 35, and 50 degrees. Right: A view looking into the aorta and coronary ostium with only the AOs of 20 and 50 degrees depicted for clarity.

2.9 Virtual Narrowing of the Proximal LMCA and Altering HMR

To mimic lateral compression of the upstream portion of the LMCA (i.e. proximal stenosis), we manually created 2D elliptical segments with smaller cross sections compared to the original model. Prior studies have reported proximal area stenoses of ~40-70 percent, with 70 percent being linked to ischemia.^{3,5,17} We therefore considered area stenoses of 60, 65 and 70 percent in this study and examined if vFFR is in agreement with the prior studies that identified these stenoses levels near the hemodynamic limit.^{3,5,17} Elliptical contours were defined through segmentation in SimVascular using control points (marked as 1 & 2 in the Figure 2.12, left) along the periphery of the contour. These control points were then moved within their imaging plane (marked as 1' & 2' in the Figure 2.12, right) to adjust minimal and maximal diameters of the ellipse until the desired stenosis level was obtained. Segments of the distal coronary artery were left untouched and the new model was then obtained by lofting the segments.

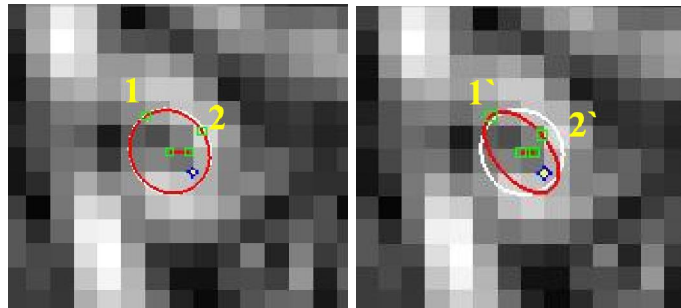


Figure 2.12. Lumen contour and corresponding control points of the original (left) and virtually constricted model (right)

In addition to the epicardial stenosis, HMR affects FFR. In agreement with the method introduced by Van de Hoef et al.⁵⁷, low, intermediate and high ranges of HMR (i.e. 1.2, 1.6 and 2.3 mmHg/cm/s) were assigned for the LMCA distal to the stenosis and distributed between LAD and LCX outlets. A total of 12 simulations were performed under stress-induced conditions for the original model along with those for the three virtual stenotic levels, and related FFR values

were reported. In order to be consistent with the measurements of Van de Hoef et al.⁵⁷, hyperemic stenosis (proximal) resistance (HSR) was calculated for each stenosis severity as the ratio of pressure drop over the stenosis to mean flow velocity distal to the stenosis. Plots of FFR-HMR at different HSR levels were calculated and compared to the measurements by Van de Hoef et al.⁵⁷

3 RESULTS

3.1 Overview

Results of the current study include assessment of the morphologic parameters including AO, diameter, ostial shape, length of intramurality as well as hemodynamic indices including TAWSS, OSI in the anomalous and normally arising coronary arteries in 6 AAOCA patients for Aim1, as well as TAWSS and OSI in virtually rotated anomalous arteries for Aim 2 and FFR in virtually compress anomalous coronary arteries for Aim 3.

3.2 Morphometric Parameters of the 3D Models

Models reconstructed from the CMR of each patient are depicted in Figure 3.1. These models provide a qualitative comparison between the anatomy of the aorta and main coronary arteries of the patients. The enlarged ostium, unroofed course and the modified AO are noticeable when comparing the pre-operative and post-unroofed models of patients 1 and 2. Pre-operatively, patient 1 had a long horizontal intramural course representative of that typically seen in AAOCA patients while patient 2 had a short vertical intramural course that ran parallel with the proximal aorta. For patient 1, post-unroofing, the ostium was located within the correct sinus and for patient 2, unroofing was performed to correct the high take-off of the LMCA. Axial and coronal CMR imaging of the aorta and anomalous LMCA for patients 1 and 2, displayed in Figure 3.2, also confirms the anatomic changes post-unroofing.

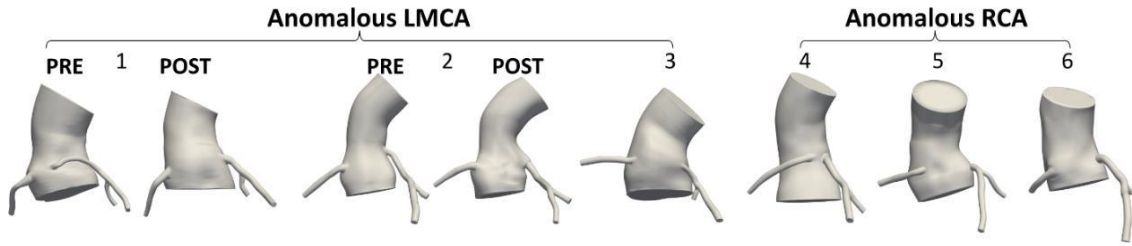


Figure 3.1 Reconstructions of the ascending aorta and coronary arteries for the six AAOCA patients studied.

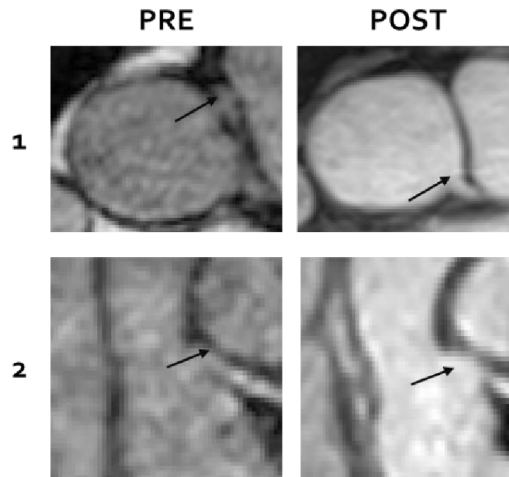


Figure 3.2 Comparison between CMR images of the patients 1 and 2, pre-operatively (PRE) and post-unroofing (POST). (Top) axial CMR indicates the anomalous LMCA originating from the right sinus that has been removed. The ostium of the unroofed LMCA is in the left sinus; (Bottom) coronal CMR indicates anomalous LMCA with a vertical course that has been removed and the patient's ostium post-unroofing.

Average diameter, AO, eccentricity index, and length of intramurality for patients 1 and 2 are listed in Table 7 and provide a quantitative comparison between the anatomy of LMCA pre-operatively and post-unroofing. For example, comparing average diameters for patient 2, $D_{PRE} = 0.23$ cm vs $D_{POST} = 0.32$ cm, confirmed ostium enlargement after unroofing. The AOs were less acute and ostial eccentricity was less elliptical post-unroofing compared to pre-operatively.

Table 7. Morphologic parameters of the LMCAs of the patients 1 and 2, pre-surgery (PRE) and post-unroofing (POST)

Patient		Flow (ml/s)	Diameter (cm)	AO (degrees)	Eccentricity Index	Length of intramurality (cm)
1	PRE	2.81	0.23	29.5	0.46	1.93
	POST	3.59	0.29	37.5	0.62	---
2	PRE	2.70	0.23	36.0	0.64	0.4
	POST	2.72	0.32	41.1	0.67	---

For patients with only post-unroofed states, average diameter and AO were computed. (Table 8). These data showed that patients 3 and 4 have more acute AO post-unroofing than the other patients studied.

Table 8. Average flow and diameter of the LMCA and RCA for all patients studied post-unroofing, along with the AO for their anomalous coronary artery.

Patient	Anomalous LMCA		Contralateral RCA		AO of the anomalous artery (degrees)
	Flow	Diameter	Flow	Diameter	
	(ml/s)	(cm)	(ml/s)	(cm)	
1	3.59	0.29	1.30	0.27	37.5
2	2.72	0.32	0.94	0.26	41.1
3	4.12	0.26	2.12	0.26	26.8

Patient	Contralateral LCMA		Anomalous RCA		AO of the anomalous artery (degrees)
	Flow	Diameter	Flow	Diameter	
	(ml/s)	(cm)	(ml/s)	(cm)	
4	2.06	0.27	0.63	0.21	25.3
5	2.44	0.28	2.43	0.26	46.3
6	3.12	0.29	1.54	0.24	37.0

3.3 Physiologic Flow and Pressure from Patient-Specific Boundary Conditions

Representative flow and pressure waveforms at the outlets of the patient 1 post-unroofed model (Figure 3.3) indicate that physiologic behavior has been captured by the BCs imposed. For example, peak blood flow in the coronary arteries during diastole confirms the phasic blood flow characteristics in these vessels. The systolic to diastolic peak ratios for the right and left coronary arteries are calculated as 0.96 and 0.05 respectively, in agreement with the previous studies.¹⁰⁸

The range of SBP and DBP from simulations were 120-123 mmHg and 63-64 mmHg, in good agreement with the measured BP of 123/64 mmHg.

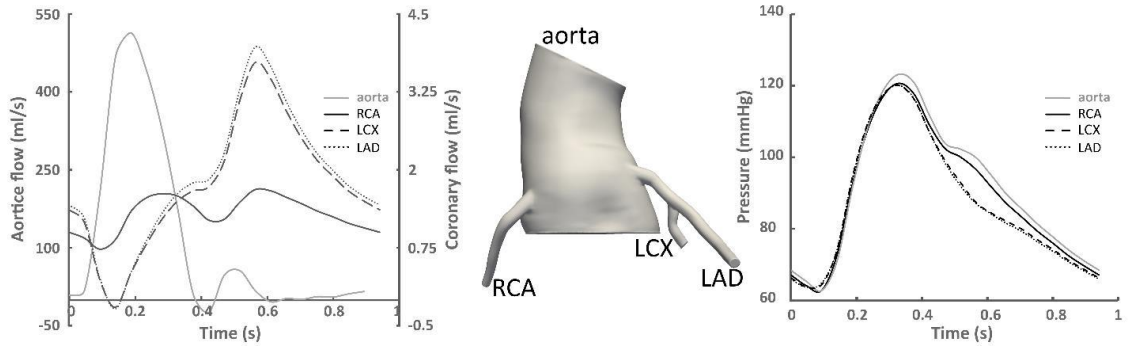


Figure 3.3 Flow and pressure waveforms for a representative AAOCA patient during one cardiac cycle.

3.4 Hemodynamic Comparison between Pre-operative and Post-unroofing States

Velocity profiles from cross-sections along the LMCA of patient 1 are depicted in Figure 3.4. The velocity profile in the pre-operative LMCA is skewed toward the outer curvature when compared to the post-unroofed case. The maximum velocity value in this region reaches 190 cm/s preoperatively and creates higher velocity gradients and WSS distributions compared to the post-unroofed model. An increased diameter relative to the unroofed state (i.e. pre 0.23 cm; post 0.29 cm) led to a lower velocity despite an increase in the CO of the post-unroofed model. The lower velocity, as well as less curvature of the proximal LMCA post-unroofing, caused less deviated velocity profiles and lower WSS magnitude with a more homogenous distribution along the inner and outer wall curvatures.

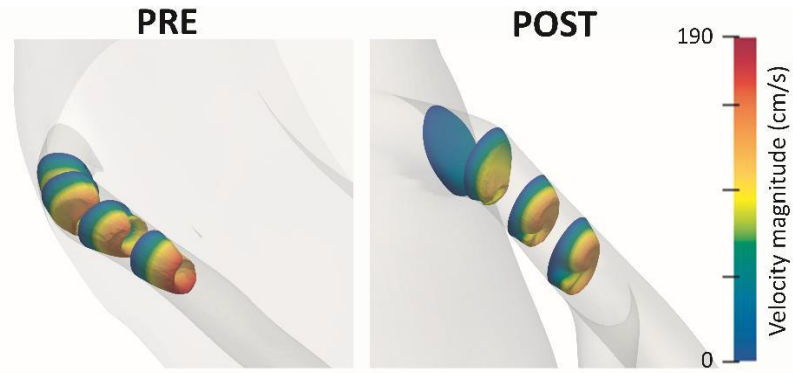


Figure 3.4 . Local diastolic velocity profiles (i.e. during peak coronary flow) along the proximal portions of the anomalous LMCA for patient 1 pre-operatively (PRE) and post-unroofing (POST). Velocity profiles are displayed at diameter multiples of the artery from the ostium. Velocity profiles of the PRE are more skewed toward the outer wall than those of the POST as a result of the curvature of the artery caused by its acute AO. Higher velocity and a lower diameter of the model pre-operatively are responsible for regions of higher wall shear stress (WSS) magnitude as reported in the figures that follow.

Collective distributions of TAWSS within the LMCA pre-operatively vs post-unroofing are shown in Figure 3.5. A reduction in TAWSS is generally observed for the post-unroofed cases. Plots of ensemble averaged longitudinal TAWSS within locations highlighted in the figure confirm TAWSS decreases locally from pre-operative to post-unroofed states. These changes reached significance on the outer walls at 1, 2, 2.5 diameters distal from the ostium (1D PRE: 239 ± 4 dyne/cm² vs POST: 103 ± 10 dyne/cm², $P=7.6e-04$; 2D PRE: 219 ± 35 dyne/cm² vs POST: 104 ± 36 dyne/cm², $P\text{-value} = 3.6e-03$; 2.5D PRE: 276 ± 28 dyne/cm² vs POST: 91 ± 15 dyne/cm², $P\text{-value} = 2.2e-02$).

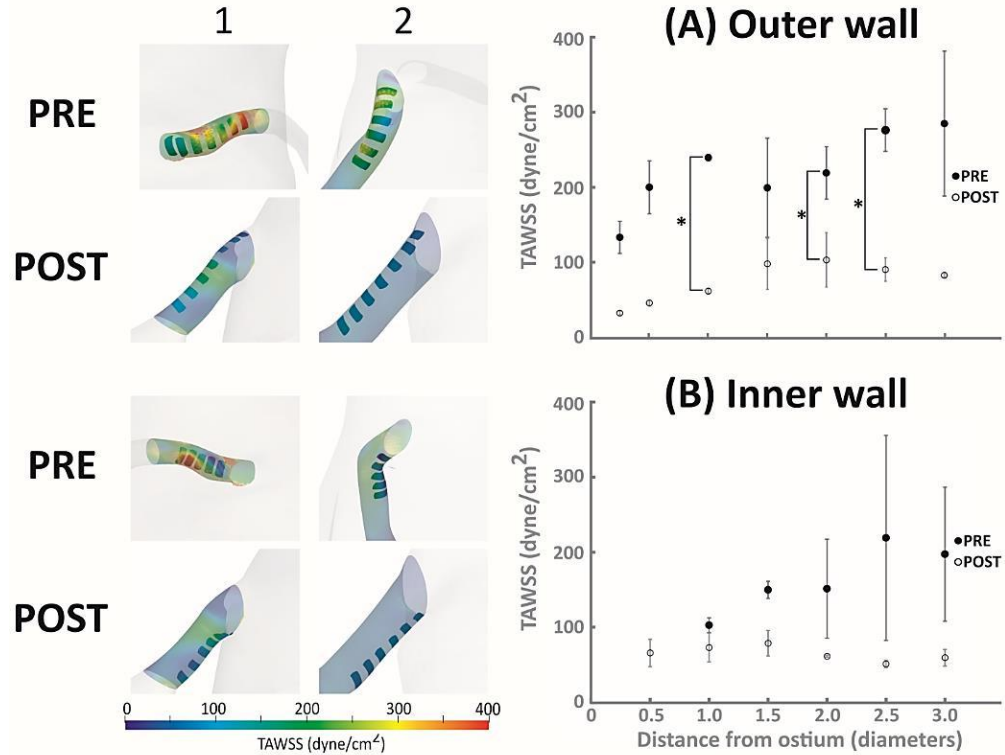


Figure 3.5 Comparison of time-averaged wall shear stress (TAWSS) pre-operatively (PRE) and post-unroofing (POST); $n=2/\text{group}$. TAWSS distributions are shown for locations along the (A) outer and (B) inner walls of the LMCA. Plots show mean \pm standard error of the mean for values within spatially equivalent locations from both patients. Regions of local quantification are located at 0.5 diameter multiples downstream from the ostia to normalize somatic difference between patients. * significant difference between PRE and POST ($P<0.05$).

Figure 3.6 shows the spatial distribution of OSI along the inner and outer walls of the anomalous LMCA pre-operatively and post-unroofing. For patient 1, modestly elevated OSI is confined to the inner luminal surfaces of the proximal LMCA. High OSI values are observed on both inner and outer luminal surfaces of the ostial region for patient 2. OSI decreases distal to the ostia. Differences between OSI distributions pre-operatively and post-unroofing were not statistically significant.

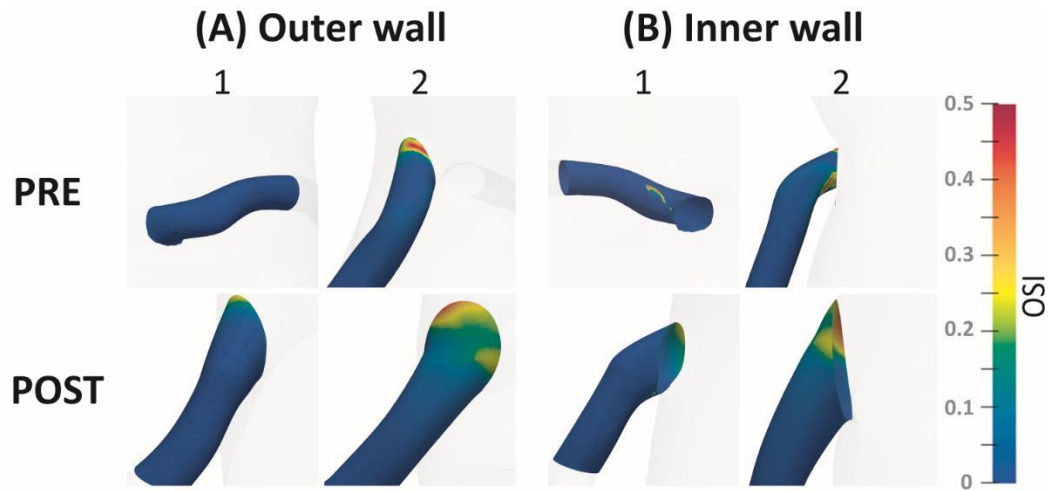


Figure 3.6 Comparison of oscillatory shear index (OSI) for the pre-operative (PRE) and post-unroofed (POST) models. OSI is shown along the (A) outer and (B) inner walls of the LMCA; n=2/group. Highest OSI values are found near the ostia of the models pre-operatively and post-unroofing, but differences between PRE and POST were not statistically significant.

3.5 Hemodynamic Comparison between Left and Right Coronary Arteries

TAWSS distributions for the contralateral normally-arising right (patients 1 - 3) and contralateral normally arising left coronary arteries (patients 4 - 6) as well as the localized quantification of TAWSS results for these patients are displayed at the upper rows of Figure 3.7A and B. There are significant regional differences (e.g. elevated TAWSS in the left coronary artery) observed along the outer wall 1.5-3 diameters distal to the ostia and on the inner wall 2.5-3 diameters distal to ostia. Comparing TAWSS between the unroofed left and right arteries (i.e. bottom rows of Figure 3.7 A and B) also reveals some regional differences. Differences were not significant due to high standard deviations introduced by patient 3, which had pronounced CO, smaller coronary artery diameters and a more acute AO relative to the other two unroofed left arteries (Table 8).

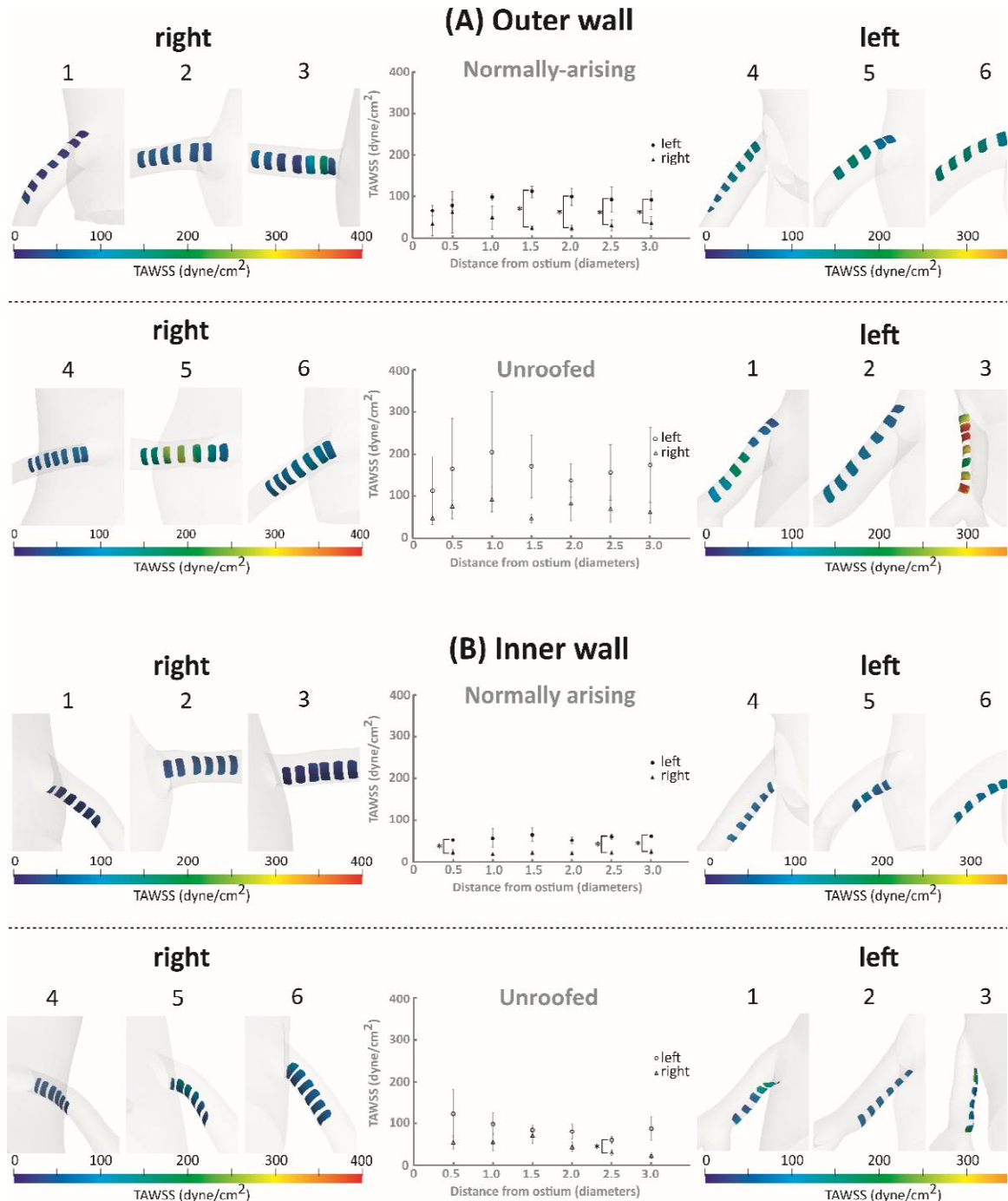


Figure 3.7 Comparison of time-averaged wall shear stress (TAWSS) between the left and right coronary arteries. TAWSS distributions are shown for locations along the (A) outer and (B) inner walls of the contralateral normally arising left and right (top) as well as the unroofed left and right (bottom) coronary arteries. Plots show mean \pm standard error of the mean from three patients with the unroofed left, i.e. contralateral normally arising right (1, 2 and 3), and three patients with the unroofed right, i.e. contralateral normally arising left (4, 5 and 6) coronary arteries. * significant difference between left and right ($P < 0.05$). Data are assumed to be normally distributed.

3.6 Hemodynamic Comparison between Unroofed and Contralateral Coronary Arteries

Longitudinal distributions of TAWSS for the normally arising and unroofed states for LMCA and RCA are shown in Figure 3.8. The results show no significant difference between the contralateral normally arising and unroofed LMCA on either inner or outer wall surfaces. Similarly, there was no significant difference between the normally arising and unroofed RCA. These data suggest that unroofing normalizes WSS with variances related to AO.

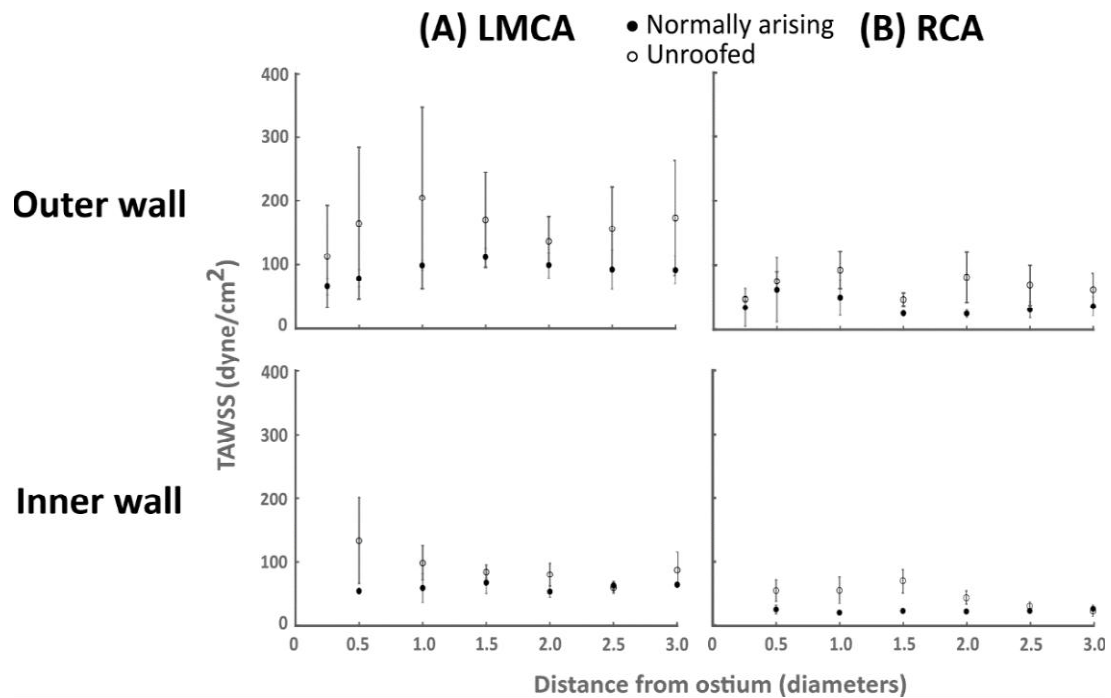


Figure 3.8 Comparison of time-averaged wall shear stress (TAWSS) between contralateral normally-arising and unroofed coronary arteries. Plots of TAWSS averaged within locations along the outer and inner walls of the contralateral normally arising and unroofed (A) LMCA, (B) RCA. There was no statistical difference between the contralateral normally arising and unroofed states. $n=3/\text{group}$ i.e. patients 1,2,3 with unroofed LMCA and contralateral RCA, patients 4, 5, 6 with unroofed RCA and contralateral LMCA. Data are assumed to be normally distributed.

Figure 3.9 provides a comparison between OSI values of the normally arising and unroofed artery as well as between the left and right coronary arteries for the post-unroofed models. Oscillations are confined to 0.5-1 diameters from the ostia and there are no significant

differences when comparing left vs right or contralateral normally arising vs unroofed coronary arteries.

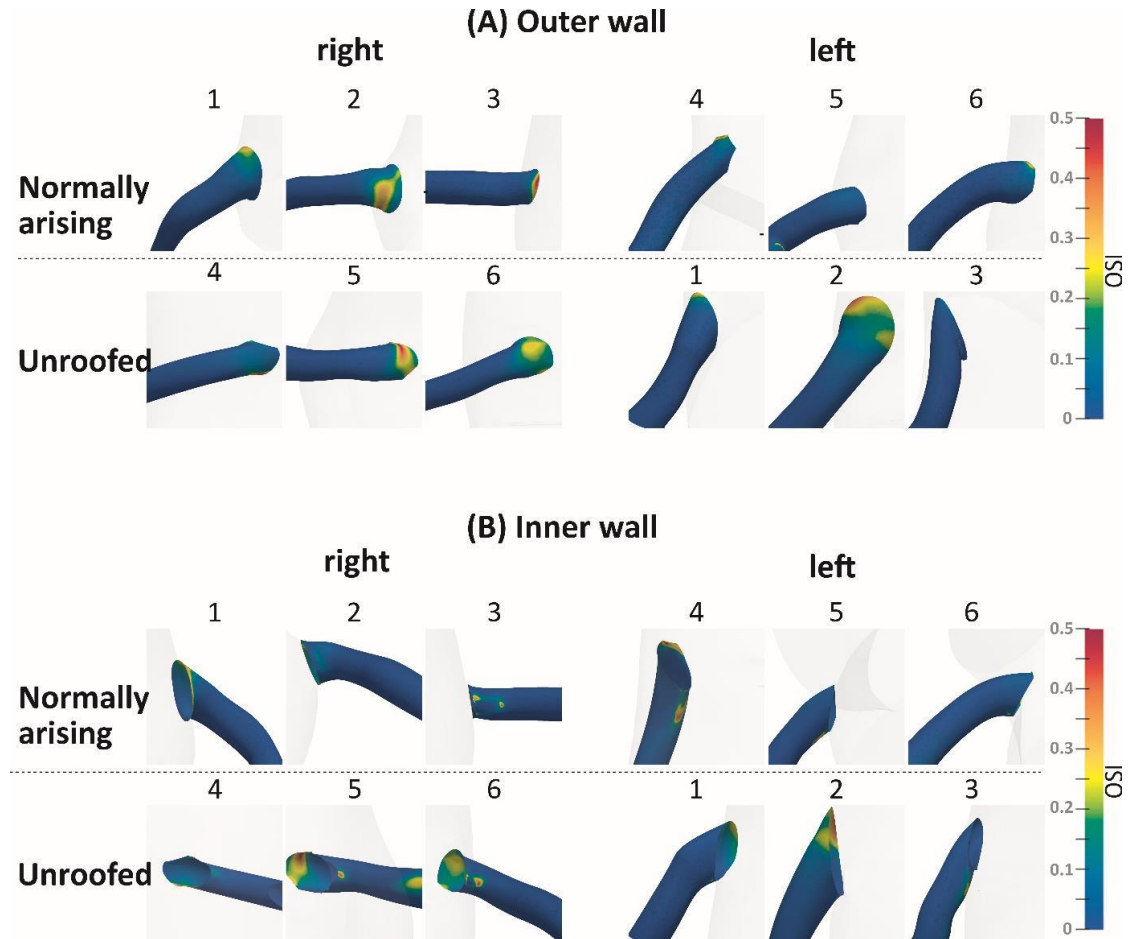


Figure 3.9 Comparison of oscillatory shear index (OSI) between the contralateral normally-arising and unroofed coronary arteries along the (A) outer and (B) inner walls; $n=3/\text{group}$ i.e. patients 1,2,3 with unroofed left and contralateral right, patients 4, 5, 6 with unroofed right and contralateral left coronary arteries. High OSI values are observed near the ostium of contralateral normally arising and unroofed models, but differences were not statistically significant.

3.7 Hemodynamic Comparison between Virtually Created Angles of Origins

TAWSS and OSI distributions for the left coronary arteries of the original as well as rotated models having AOs of 20, 30, 35, 50 degrees, and the quantification of TAWSS and OSI

results within circumferential regions located on the outer and inner walls of the LMCA are represented in Figure 3.10 and

Figure 3.11. ANOVA revealed a statistically significant difference between mean TAWSS and OSI on the outer and inner walls of LMCA with different AO. Pots-hoc Tukey test showed a significant difference for simulations with different AOs at almost all the diameter multiples along the outer wall as well as some portions along the inner wall. The outer wall in the proximity of the ostium experienced lower TAWSS and higher OSI at more acute AO. At the inner wall, TAWSS comparison revealed that the differences were generally consistent along the length of the vessel; however, OSI values did not consistently change along the vessel length for different AO models.

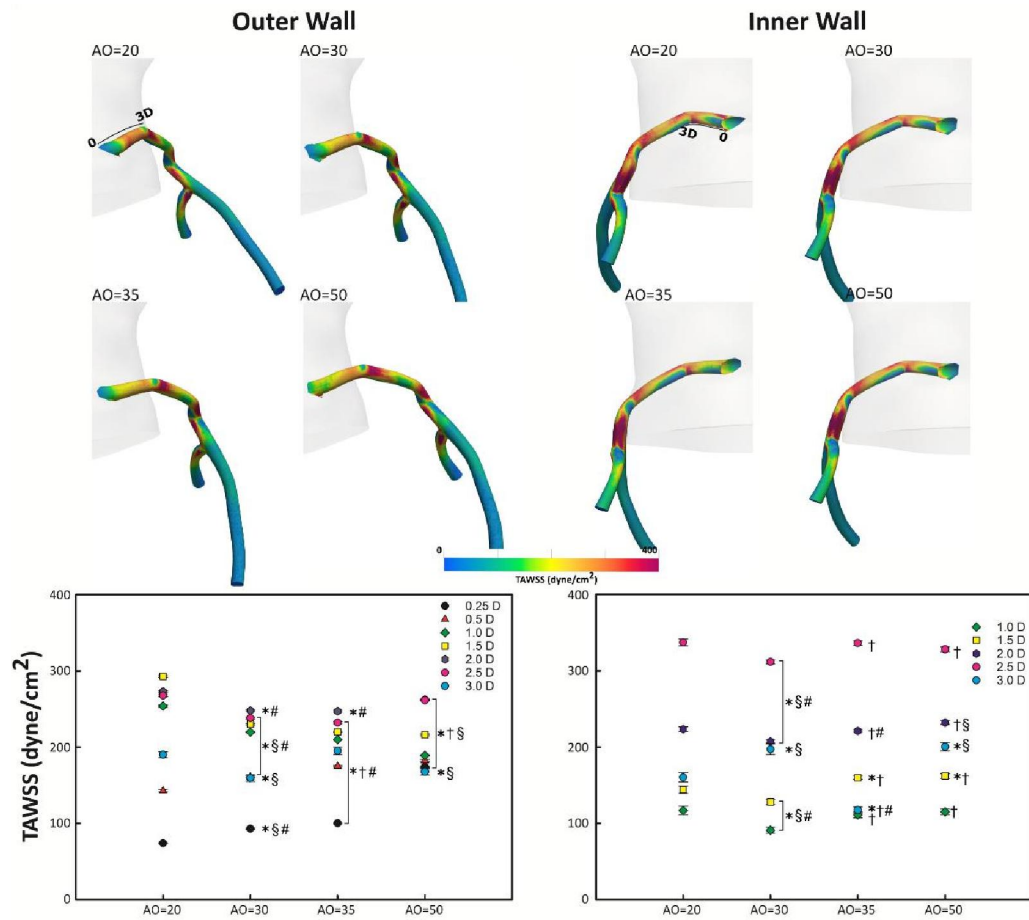


Figure 3.10 (Top) Contour representation of TAWSS on the outer and inner walls of the left coronary artery and (Bottom) plots of TAWSS calculated on the inner and outer wall within circumferential bands at diameter multiples from the left coronary ostia for four AOs. Values show mean \pm standard error of the mean. Significantly different ($P < 0.05$) from mean TAWSS within bands of *AO=20 degrees, †AO=30 degrees, § AO=35 degrees, and # AO=50 degrees.

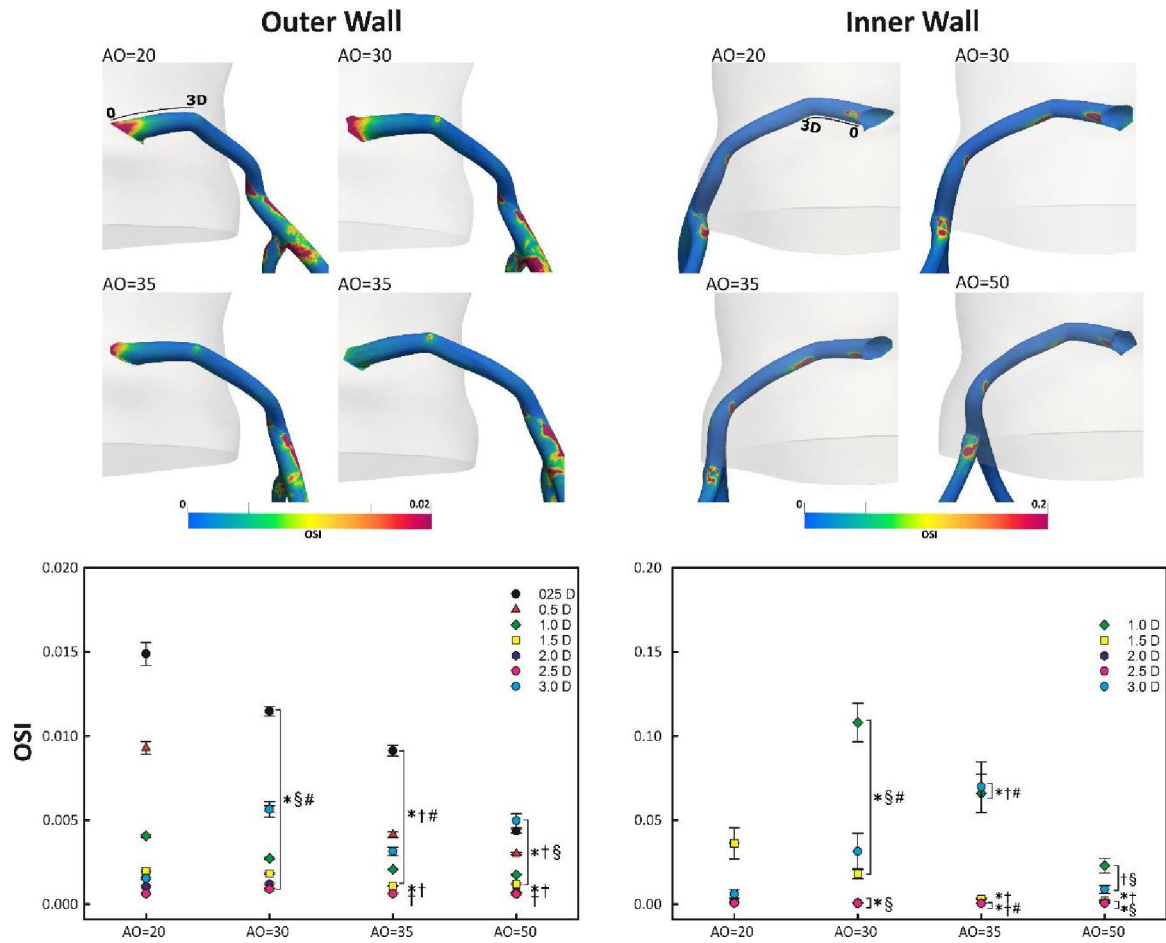


Figure 3.11 (Top) Contour representation of OSI on the outer and inner walls of the left coronary artery and (Bottom) plots of OSI calculated on the inner and outer wall within circumferential bands at diameter multiples from the left coronary ostia for four AOs. Values show mean \pm standard error. Significantly different ($P < 0.05$) from mean TAWSS within bands of *AO=20 degrees, †AO=30 degrees, § AO=35 degrees, and # AO=50 degrees.

3.8 FFR Analysis in Virtually Compressed Anomalous Artery

Figure 3.12 shows a schematic of the anomalous LMCA of the original and virtually compressed (stenosis) model, as well as the proximal and distal cross-sections over which the pressure was averaged to calculate vFFR.

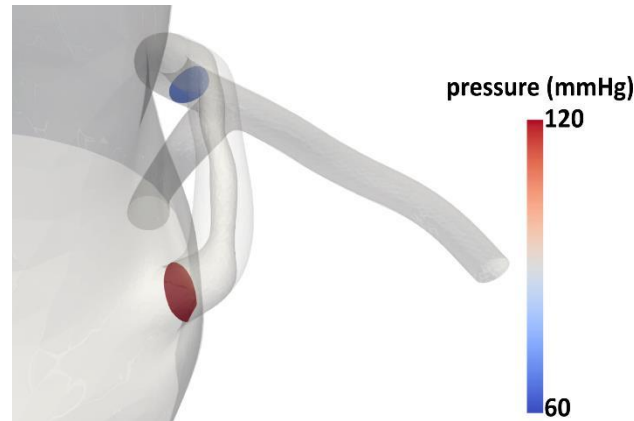


Figure 3.12 Intramural LMCA of the representative and virtually compressed model. Pressure was averaged within the cross-sections proximal and distal to the compressed region to calculate FFR

As mentioned in the methods section, proximal resistance (i.e. stenosis severity) of the LMCA is characterized by HSR. Table 9 shows vFFR values for the equivalent HSR of the original and virtually compressed models at HMR values of 1.2, 1.6 and 2.3 mmHg/cm/s. Figure 3.13 plots vFFR-HMR at each HSR value and compares vFFR to the measured FFR from Ven de Hoef et al⁵⁷ for the similar range of HMR and HSR. At higher proximal resistance, vFFR is lower as expected. All virtually compressed models show a significant FFR independent of HMR. However, for a certain HSR, vFFR also tends to increase with increasing HMR. This results in similar FFR to be observed for different proximal resistance values depending on HMR. For example, vFFR at HSR:1.0-1.3 and HMR: 2.30 mmHg/cm/s is 0.69 and similar to vFFR at HSR:0.6-0.7 and HMR: 1.6 mmHg/cm/s. Overall, these vFFR data are in good agreement with measurements by Ven de Hoef et al⁵⁷ for the given HMR and HSR ranges.

Table 9 vFFR calculated for the original and three virtually compressed models. Units of HMR and HSR are mmHg/cm/s. Compression levels (stenosis severities) show luminal area reduction.

	Original (HSR: 0.1-0.2)	60% (HSR: 0.6-0.7)	65% (HSR: 0.8-1.0)	70% (HSR: 1.0-1.3)
HMR	vFFR			
1.20	0.88	0.62	0.55	0.49
1.60	0.91	0.70	0.64	0.58
2.30	0.95	0.79	0.74	0.69

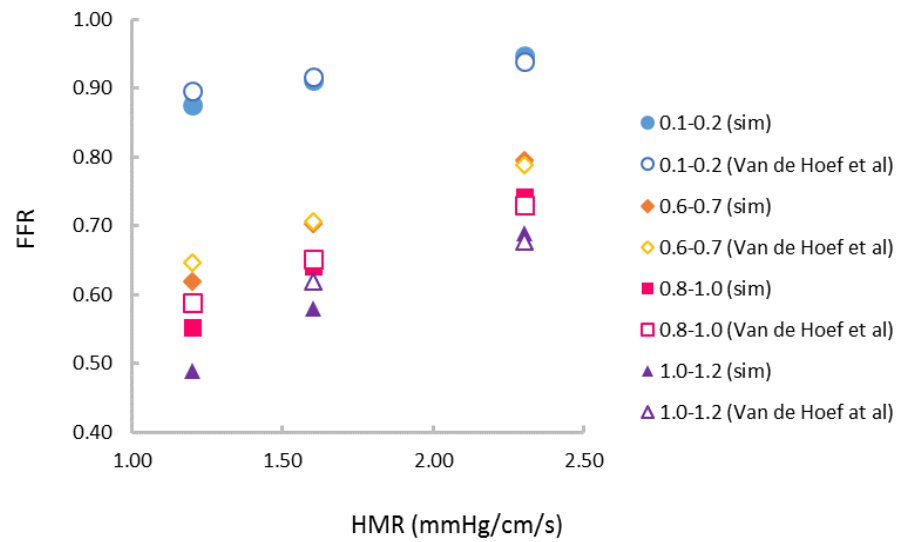


Figure 3.13 Comparison between vFFR and measured FFR by Van de Hoef et. al⁵⁷ for the similar range of distal microvascular (HMR) and proximal resistances (HSR). vFFR shows an increasing trend with increasing HMR for a given proximal resistance. (FFR data at HMR 1.2 mmHg/cm/s and HSR (1-1.2) mmHg/cm/s was not reported by Van de Hoef et. al)

4 DISCUSSION

4.1 Overview

CFD modeling is a method of simulating fluid passing through or around an object, in this case blood vessels, by replacing the governing partial differential equations with algebraic equations that can be solved numerically. Indices of WSS attainable through CFD have previously helped to characterize the impact of blood flow distributions on the vascular adaptation.^{34,109,110}

The current study represents the first image-based patient-specific CFD modeling of blood flow patterns in the coronary arteries of 6 AAOCA patients. The associated simulations used a previously developed multi-scale modeling approach that coupled 3D reconstructed models to 0D LPN models prescribed as outlet BCs. The LPN models included the effect of the downstream vascular networks not included in the 3D domain due to image resolution or computational expense. Parameters of the coronary LPN models that capture cardiac contraction and relaxation, as well as coronary microcirculation, were determined under resting (for Aims 1 & 2) and simulated stress (i.e. exercise) conditions (for Aim 3) using a robust protocol to identify hemodynamics with a high level of realism. Velocity patterns, pressure, and WSS results from these simulations were then analyzed and compared between unroofed and contralateral normally arising coronary arteries in post-unroofing models, between pre-operative and post-unroofed models as well as between either left and right normally arising and left-right unroofed coronary arteries. These data led to examine the impact of unroofing in normalizing hemodynamics and to evaluate the effects of blood flow and geometry on resulting WSS indices including TAWSS and OSI. These indices are the most commonly used hemodynamic parameters in computational cardiovascular studies with well-established relation with vascular pathologies.²⁵ Effects of AO and lateral compression of the anomalous artery, as potential contributing factors in AAOCA morbidity and ischemia, were analyzed through virtual creation of these states by morphing a

representative pre-operative model. Indices of WSS and FFR were assessed to predict high-risk anatomies.

4.2 Summary of Findings from Aim 1

Comparison of AO and eccentricity index between pre-operative and post-unroofed states showed some improvement after unroofing (e.g. patient 1 AO: 29.5° PRE vs 37.5° POST, eccentricity index: 0.46 PRE vs 0.62 POST). However, post-unroofed data were not representative of a rounded normally arising ostia. For the rest of the post-unroofed models, similar observations were confirmed. For example, the post-unroofed LMCA of patient 3 or post-unroofed RCA of patient 4 still included an acute AO. These data, in accordance with prior studies¹¹¹ suggest that the results from unroofing surgery may not perfectly mimic a native coronary ostium or its AO.

Differences in TAWSS suggest intrinsically different flow patterns between right and left coronary arteries in their native state (Figure 3.7). This resulted in higher local distributions of TAWSS for the contralateral normally arising left coronary arteries for several segments along the outer and inner walls of curvature. There was also a trend toward higher TAWSS in unroofed left vs unroofed right coronary arteries. This might be partially due to differences in flow rates for each artery, although in general, vessels within a given vascular region tend to be centered around a preferred range of values consistent with biomechanical homeostasis.¹¹² The difference in TAWSS values between normally arising left vs right coronaries arteries is thus potentially surprising and may warrant further investigation in a larger cohort. It is also important to note that both contralateral normally arising and unroofed vessels are affected by systolic and diastolic alterations in WSS. Different extramural pressures imposed from the left and right ventricles were included in our models through the incorporation of separate intramyocardial pressure waveforms (i.e. $P_{im,left}$ & $P_{im,right}$). These waveforms lead to the asynchrony between the left and right

coronary flows as well as the velocity gradients that result in WSS distributions. A lower distal pressure in the left compared to the right coronary arteries seen in the Figure 3.3 is a result of higher left end diastolic pressure, in agreement with prior studies.¹¹³

Our results for the entire cohort of unroofed vs contralateral normally arising coronary arteries indicate no significant differences (Figure 3.8). This suggests that the unroofing surgery may alter the WSS by normalizing it, with variance that seems at least partially related to the AO of the anomalous coronary artery post-unroofing. However, as mentioned previously, larger cohort studies are needed. It is also worth noting that we do not have access to truly ‘normal’ coronary arteries from healthy age and gender matched controls at the current time. This limited our results to the comparison between unroofed and contralateral normally arising arteries among the current patients.

The physiologic range of WSS has not been measured for pediatric populations. However, overall our simulated WSS data suggest a higher range of WSS compared to those in adults³⁵ due to the smaller vessel sizes. Our results showed that WSS was decreased and normalized post-unroofing. Additional clinical studies are required to measure the gold standard values for WSS which can be used to examine the impact of this normalization and efficacy of the unroofing procedure.

TAWSS significantly decreased from the pre-operative period in the 2 patients presented (both left AAOCA) after unroofing (Figure 3.5). This may be partially due to the increased average diameter as a result of the patent ostium created post-unroofing. Additionally, it should be noted that velocity profiles have more skewing towards the curved walls of the anomalous artery pre-operatively leading to higher velocity gradients, hence higher WSS. The skewed velocity profiles may also be related to the difference between AOs. The hypothesis of the role of AO in altering hemodynamics was therefore examined in aim 2.

4.3 Summary of Findings from Aim 2

Distributions of WSS depend on the local blood flow patterns impacted by the morphology of the vessel and downstream resistance. It is known that WSS is generally related to the rate of blood flow and inversely related to the diameter.¹¹⁴ However, the effect of morphological parameters was not directly attainable because of the confounding effects of flow and diameters among the models from each patient. To analyze the exclusive effect of AO, as the morphologic parameter of interest, the anomalous LMCA of a representative model was virtually rotated keeping the inlet flow and outlet BCs consistent. AO values for the representative model and three virtually created models were 30, 20, 35 and 50 degrees, respectively. Our results revealed that changes in AO led to significant alterations in the local flow patterns and hemodynamics. On the outer wall at the regions near the ostia, lower TAWSS were observed for more acute AO. At distal regions, lower TAWSS was observed for less acute AO. On the inner wall, there was a significant difference between TAWSS of different AO models and changes followed a consistent trend along the length of the vessel.

Collectively these findings suggest that acute AO creates abnormal coronary flow patterns and hemodynamics that could leave patients more susceptible to the early onset and progression of atherosclerosis and ultimately may help explain myocardial morbidity associated with intramural AAOCA.²⁵ These data also provide new insights into the importance of functional assessment and their potential for use alongside anatomical assessment to improve clinical decision making. Furthermore, this approach can be extended to virtual morphing of the post-unroofed arteries to evaluate efficacy of the unroofing and to suggest the optimum AO predictive of favorable hemodynamics.

4.4 Summary of Findings from Aim 3

Our results predicted significant vFFR for the proximal stenoses studied in agreement with the FFR measurements by Agrawal et al.¹⁷ in the anomalous coronary arteries of the children with $\geq 70\%$ luminal narrowing. Our findings show that FFR decreases with increasing HSR (i.e. proximal narrowing) of the anomalous artery. As predicted, the original model (i.e. no-stenosis) showed the lowest HSR and the highest stenosis severity showed the highest HSR. In addition to stenosis severity, FFR values are also affected by the downstream resistance (i.e. HMR). When HMR was lower, FFR values were also lower for a given HSR. Lower HMR means the resistance to coronary flow is low at the downstream vasculature. Therefore, more blood flow passes through the artery. When the blood flow passing a stenosis increases, the pressure-drop over the stenosis increases, thus FFR will be lower.¹¹⁵ Similarly, despite the flow impediments induced by high HMR, a higher FFR was obtained for a given HSR. Our findings agreed well with the measured FFR, HSR and HMR in 228 patients with 299 coronary stenoses by Van de Hoef et al.⁵⁷ For instance, for the original model, i.e. HSR (0.1-0.2) mmHg/cm/s, simulated vFFR values were 0.88, 0.91 and 0.95 for HMR values of 1.2, 1.6 and 2.3 mmHg/cm/s respectively (see Figure 3.13). These vFFR values compared well with their measured FFR values of 0.9, 0.92 and 0.94 for the similar HMR and HSR range. The difference between our simulated vFFR and their measured FFR slightly increased for the low HMR at higher HSR ranges. For example, for the 65% area stenosis (i.e. HSR (0.8-1.0) mmHg/cm/s) simulated vFFR values were 0.55, 0.64 and 0.74 compared to their measured FFR of 0.59, 0.65 and 0.73 for HMR values of 1.2, 1.6 and 2.3 mmHg/cm/s, respectively, showing the maximum difference of 6% at $HMR \approx 1.2$. Our findings may predict the anatomies with hemodynamic significance based on classic FFR criteria. Moreover, they reinforce the interplay between HMR and HSR in regulating FFR and suggest that functional assessment of anomalous coronary arteries through FFR may need to be revisited considering the impact of the vascular resistance distal to the narrowing. In the clinical setting,

different levels of microvascular resistance (i.e. HMR) could be obtained through Doppler echocardiography under different levels of stress-testing (e.g. exercise or various doses of Dobutamine stress) and the corresponding vFFR data for a given patients HSR could then be calculated to provide a non-invasive functional assessment of AAOCA. Ultimately, further studies in a larger population using the current methods will allow us to evaluate possible correlations between prevalence of ischemia and HMR-based vFFR, and ultimately improve understanding of risk stratification in intramural AAOCA patients.

4.5 Limitations, Computational Considerations and Future Directions

In this section, we discuss the limitations and computational modeling considerations that can impact the results presented.

One of the main limitations of the current study is the small sample size. From the patients in the current study, only two had both pre-operative and post-unroofing data as it was not the standard of care to perform pre-op MRIs at the time this study was initiated. Small sample size may limit the accuracy of statistical inference. Future studies with a larger cohort will allow for a correlation analysis between hemodynamic indices and patient outcomes to predict the patients' future risk for ischemia or morbidity. Important computational considerations in modeling, execution and data analysis include patient-specific geometry, inlet and outlet BCs, valve dynamics, deformable walls, cardiac motion, computational time as well as the verification and analysis of the results.

Many modern software packages can create patient-specific geometric representations from volumetric imaging data, and we used SimVascular for this purpose. The 3D reconstructed models were confirmed to be representative by collaborating clinicians considering the resolution and the software capability. The current study also employed a robust protocol to determine parameters for the outlet BCs applied at the aortic and coronary outlets. This was necessary to

realistically replicate the out-of-phase nature between flow and pressure in the coronary arteries. This is an important point as many studies modeling the aorta and coronary arteries still use simplified approaches of imposed inflow and outflow waveforms that do not allow for patient-specific and/or realistic pressure fields within the computational results. Even for simple geometries, incorrect choice of BCs leads to completely different flow distributions and inaccurate wall deformation in fluid structure interaction (FSI) simulations.^{101,116} In contrast, the multi-scale modeling approach implemented in SimVascular for the current work allows for some of the most realistic CFD simulations results available to date, and for the first time in AAOCA patients, by considering the effects of cardiac contraction and relaxation with BCs that can be implemented based on available patient data. However, it is not currently possible to include the physical aortic valve and its movement with SimVascular. Nonetheless, the realistic BCs that were implemented in the current work do result in temporally varying physiologic pressure gradients within the model that establish the conditions for flow to each of the coronary arteries and aorta, albeit without the physical valve present or moving. Prior research in our lab was able to include the movement of the aortic valve using a commercial software package and simplified material properties.¹¹⁷ However, this prior work applied waveforms at the outlets of models that were not patient-specific. These prior simulations also did not include the coronary arteries with their unique phasic behavior or outlet BCs that accounted for cardiac function. Moreover, implementation of valve motion requires accurate and patient-specific characterization of valve material properties. There is a paucity of such experimental data in the literature and the authors are not aware of a way to non-invasively estimate patient-specific material properties from current clinically available imaging modalities.

Healthy arteries are indeed pulsatile, which suggests deformability in the form of FSI simulations should be conducted in the setting of healthy aortas. However, deformation of normal coronary arteries is more modest (approximately 2% for normal adults¹¹⁸) and studies have indicated that differences in TAWSS and OSI between FSI and rigid wall simulations in the

coronary arteries are not significant.⁴² Any differences in TAWSS or OSI between FSI and rigid wall simulations is likely to be less pronounced in the setting of disease, which has a tendency to stiffen arterial tissue. There is currently lack of data on deformation of the coronary arteries for children and young adults that could have been taken into consideration for the current study. These data, once ultimately available, will provide additional information on the impact of FSI simulations between the adults and pediatric population. Specific to AAOCA, there are data to indicate that arterial compression has a role in subsequent ischemia. Implementing this detail would require knowing the arterial material properties for each patient, and an ability to define contact between the coronary arteries and surrounding structures. Currently the material properties of coronary arteries from AAOCA patients are not known, and general contact algorithms for use with FSI simulations are only available in commercial solvers that do not include realistic BCs natively. In our opinion, estimating material properties of the coronary arteries of AAOCA patients and mimicking the compression of these arteries with a commercial solver having poor BCs would likely be fraught with potentially even greater uncertainty than the current approach that uses realistic BCs with patient-specific geometries.

Motion of the coronary arteries due to cardiac contraction and relaxation was not considered in the current study. The effect of coronary artery movement has been shown to be secondary not affecting hemodynamics as much as the geometry, dynamic inflow and BCs.^{119–121}

Although outlet BCs and the aortic waveforms implemented were patient-specific, the inflow BC employed used a parabolic velocity profile. Patient-specific velocity profiles can be obtained through three component PC-MRI. However, the use of this technique in the clinical setting is challenging since it requires proper in-plane and through-plane velocity encoding, appropriate sampling to avoid noise and aliasing as well as specialized sequences.¹²² Youssefi et al¹²³ studied the impact of inlet velocity profile on the hemodynamics of the thoracic aorta. Their results showed that the choice of the inlet velocity had a significant effect in the ascending aorta and the patient-specific inflow had some similarities with the parabolic inflow compared to that

with the plug inflow. With this in mind, our future work should include a sensitivity analysis to examine the effect of the inlet velocity profile on the coronary artery flow patterns for these patients. It is also worth noting that the aortic inflow PC-MRI measurements were performed at the sinotubular junction which is distal to the coronary artery origin. This limitation underestimates coronary inflow rate compared to the 2D PC flow obtained within the aortic sinuses.¹²⁴

The total simulation time for the modeling, meshing and execution require multiple days, varies among the models, and is impacted by image resolution, complexity of the geometry, software capability, operator experience, run time limit, and the availability, speed and functionality of the HPC system being used. Near real time use of simulation results is not feasible up to date for AAOCA and the significant required time to perform hemodynamic analysis has also limited the use of patient-specific CFD in routine clinical care in many cases. Advances in parallel computing and automated workflows for the image segmentation and parameter estimation via machine learning tools along with related advances in the modeling process will help to overcome these challenges and speed up the solution time.

A robust verification and validation study were beyond the scope for the current work. In future studies, simulation results can be verified by the clinical metrics obtained from 4D flow MRI, 2D PC-MRI at a given cross-section or along the length of vessels, or spectral Doppler measurements from ultrasound. However, the accuracy of these techniques can also be limited by the as spatial and temporal resolution employed. Detailed hemodynamics resolved by a properly refined mesh size as part of numerical simulations may not be captured by the limited voxel/pixel sizes of the 4D flow or 2D PC-MRI, and these direct measurements were not available for all patients in the current study. Moreover, the agreement between our vFFR values with the clinically measured FFR⁵⁷ can be also considered a form of validation or vote of confidence in the accuracy of our simulations.

As mentioned previously, we analyzed two WSS indices because of their well-known relation to vascular pathologies. Additional WSS indices have been shown to be related to the initiation and progression of atherosclerosis. For example, helical flow intensity has been introduced to have an atheroprotective role against wall thickening.¹²⁵ Moreover, besides OSI, other multidirectional WSS indices such as particle residence time or transverse WSS has been associated with plaque formation.¹²⁶ These indices are to be used as additional markers beyond TAWSS and OSI in future hemodynamic assessment of the coronary arteries of AAOCA patients.

4.6 Conclusion

In conclusion, differences in TAWSS suggest intrinsically different flow patterns between right and left coronary arteries in their native state. Unroofing surgery normalizes TAWSS but with variance that seems at least partially related to the AO of the anomalous coronary post-unroofing. Differences in TAWSS and OSI for virtually rotated models suggest AO significantly impacts coronary hemodynamics. Analysis of vFFR suggests that functional assessment of a proximal narrowing from compression of the anomalous artery should include the effect of downstream resistance in predicting ischemia. Collectively this study supports the use of methods employed for larger scale studies of AAOCA that could correlate these findings with outcomes, especially for appropriate risk stratification if anatomic or flow-related coronary or myocardial perfusion abnormalities are identified.

BIBLIOGRAPHY

1. Taylor AJ, Rogan KM, Virmani R. Sudden cardiac death associated with isolated congenital coronary artery anomalies. *Journal of the American College of Cardiology*. 1992;20(3):640–647
2. Lim JCE, Beale A, Ramcharitar S. Anomalous origination of a coronary artery from the opposite sinus. *Nature Reviews Cardiology*. 2011;8(12):706–719.
3. Lee SE, Yu CW, Park K, Park KW, Suh JW, Cho YS, Youn TJ, Chae IH, Choi DJ, Jang HJ, Park JS, Na SH, Kim HS, Kim KB, Koo BK. Physiological and clinical relevance of anomalous right coronary artery originating from left sinus of Valsalva in adults. *Heart*. 2016;102(2):114–119.
4. Agrawal H, Mery CM, Day PE, Sexson Tejtzel SK, McKenzie ED, Fraser CD, Qureshi AM, Molossi S. Current practices are variable in the evaluation and management of patients with anomalous aortic origin of a coronary artery: Results of a survey. *Congenital Heart Disease*. 2017;12(5):610–614.
5. Angelini P, Uribe C, Monge J, Tobis JM, Elayda MA, Willerson JT. Origin of the right coronary artery from the opposite sinus of Valsalva in adults: Characterization by intravascular ultrasonography at baseline and after stent angioplasty. *Catheterization and Cardiovascular Interventions*. 2015;86(2):199–208.
6. Boler AN, Hilliard AA, Gordon BM. Functional assessment of anomalous right coronary artery using fractional flow reserve: An Innovative Modality to Guide Patient Management. *Catheterization and Cardiovascular Interventions*. 2017;89(2):316–320.
7. Iaizzo PA. *Handbook of cardiac anatomy, physiology, and devices, third edition.*; 2015.
8. Muller-Delp JM. The Coronary Microcirculation in Health and Disease. *ISRN Physiology*. 2013.
9. Westerhof N, Boer C, Lamberts RR, Sipkema P. Cross-talk between cardiac muscle and coronary vasculature. *Physiological Reviews*. 2006.
10. Duncker D, Bache R. Regulation of coronary blood flow during exercise. *Physiological reviews*. 2008;88:1009–1086
11. De Bruyne B, Oldroyd KG, Pijls NHJ. Microvascular (Dys)Function and Clinical Outcome in Stable Coronary Disease. *Journal of the American College of Cardiology*. 2016.
12. Reul RM, Cooley DA, Hallman GL, Reul GJ. Surgical treatment of coronary artery anomalies: Report of a 371/2-year experience at the Texas Heart Institute. *Texas Heart Institute Journal*. 2002.
13. Saul P, Gajewski K. Sudden cardiac death in children and adolescents (excluding Sudden Infant Death Syndrome). *Annals of Pediatric Cardiology*. 2010.
14. Frescura C, Basso C, Thiene G, Corrado D, Pennelli T, Angelini A, Daliento L. Anomalous origin of coronary arteries and risk of sudden death: A study based on an

- autopsy population of congenital heart disease. *Human Pathology*. 1998;29(7):689–695.
15. Cheezum MK, Liberthson RR, Shah NR, Villines TC, O’Gara PT, Landzberg MJ, Blankstein R. Anomalous Aortic Origin of a Coronary Artery From the Inappropriate Sinus of Valsalva. *Journal of the American College of Cardiology*. 2017;69(12):1592–1608.
 16. D. CM, M. DECC, A. MH. Sudden Death as a Complication of Anomalous Left Coronary Origin From the Anterior Sinus of Valsalva . *Circulation*. 1974;50(4):780–787.
 17. Agrawal H, Molossi S, Alam M, Sexson-Tejtel SK, Mery CM, McKenzie ED, Fraser CD, Qureshi AM. Anomalous Coronary Arteries and Myocardial Bridges: Risk Stratification in Children Using Novel Cardiac Catheterization Techniques. *Pediatric Cardiology*. 2017;38(3):624–630.
 18. Peñalver JM, Mosca RS, Weitz D, Phoon CKL. Anomalous aortic origin of coronary arteries from the opposite sinus: A critical appraisal of risk. *BMC Cardiovascular Disorders*. 2012;12.
 19. Maria Formato G, Lo Rito M, Auricchio F, Frigiola A, Conti M. Aortic Expansion Induces Lumen Narrowing in Anomalous Coronary Arteries: A Parametric Structural Finite Element Analysis. *Journal of Biomechanical Engineering*. 2018;140(11):111008.
 20. Mumtaz MA, Lorber RE, Arruda J, Pettersson GB, Mavroudis C. Surgery for anomalous aortic origin of the coronary artery. *Annals of Thoracic Surgery*. 2011.
 21. Frommelt PC, Sheridan DC, Berger S, Frommelt MA, Tweddell JS. Ten-year experience with surgical unroofing of anomalous aortic origin of a coronary artery from the opposite sinus with an interarterial course. *Journal of Thoracic and Cardiovascular Surgery*. 2011;142(5):1046–1051.
 22. Frommelt PC, Sheridan DC, Berger S, Frommelt MA, Tweddell JS. Ten-year experience with surgical unroofing of anomalous aortic origin of a coronary artery from the opposite sinus with an interarterial course. *Journal of Thoracic and Cardiovascular Surgery*. 2011;142(5):1046–1051.
 23. Nguyen AL, Haas F, Evens J, Breur JMPJ. Sudden cardiac death after repair of anomalous origin of left coronary artery from right sinus of Valsalva with an interarterial course: Case report and review of the literature. *Netherlands Heart Journal*. 2012.
 24. Sachdeva S, Frommelt MA, Mitchell ME, Tweddell JS, Frommelt PC. Surgical unroofing of intramural anomalous aortic origin of a coronary artery in pediatric patients: Single-center perspective. *Journal of Thoracic and Cardiovascular Surgery*. 2018;155(4):1760–1768.
 25. Feldman CL, Stone PH. Intravascular hemodynamic factors responsible for progression of coronary atherosclerosis and development of vulnerable plaque. *Current Opinion in Cardiology*. 2000;15(6):430–440.
 26. Zarins CK, Giddens DP, Bharadvaj BK, Sottiurai VS, Mabon RF, Glagov S. Carotid bifurcation atherosclerosis. Quantitative correlation of plaque localization with flow

- velocity profiles and wall shear stress. *Circulation Research*. 1983;53(4):502–514.
27. Dolan JM, Kolega J, Meng H. High wall shear stress and spatial gradients in vascular pathology: A review. *Annals of Biomedical Engineering*. 2013.
 28. Briguori C, Anzuini A, Airolidi F, Gimelli G, Nishida T, Adamian M, Corvaja N, Di Mario C, Colombo A. Intravascular ultrasound criteria for the assessment of the functional significance of intermediate coronary artery stenoses and comparison with fractional flow reserve. *American Journal of Cardiology*. 2001.
 29. Yang D, Kuang H, Zhou Y, Cai C, Lu T. Height, VKORC1 1173, and CYP2C9 Genotypes Determine Warfarin Dose for Pediatric Patients with Kawasaki Disease in Southwest China. *Pediatric Cardiology*. 2019.
 30. Blazek J. Chapter 2 - Governing Equations. In: Blazek JBT-CFDP and A (Second E, ed. Oxford: Elsevier Science; 2005:5–28.
 31. Arzani A, Shadden SC. Characterizations and Correlations of Wall Shear Stress in Aneurysmal Flow. *Journal of Biomechanical Engineering*. 2016.
 32. Sankaran S, Esmaily Moghadam M, Kahn AM, Tseng EE, Guccione JM, Marsden AL. Patient-Specific Multiscale Modeling of Blood Flow for Coronary Artery Bypass Graft Surgery. *Annals of Biomedical Engineering*. 2012;40(10):2228–2242.
 33. Grande Gutierrez N, Mathew M, McCrindle BW, Tran JS, Kahn AM, Burns JC, Marsden AL. Hemodynamic variables in aneurysms are associated with thrombotic risk in children with Kawasaki disease. *International Journal of Cardiology*. 2019.
 34. Han D, Starikov A, Hartaigh B, Gransar H, Kolli KK, Lee JH, Rizvi A, Baskaran L, Schulman-Marcus J, Lin FY, Min JK. Relationship between endothelial wall shear stress and high-risk atherosclerotic plaque characteristics for identification of coronary lesions that cause ischemia: A direct comparison with fractional flow reserve. *Journal of the American Heart Association*. 2016.
 35. Samady H, Eshtehardi P, McDaniel MC, Suo J, Dhawan SS, Maynard C, Timmins LH, Quyyumi AA, Giddens DP. Coronary artery wall shear stress is associated with progression and transformation of atherosclerotic plaque and arterial remodeling in patients with coronary artery disease. *Circulation*. 2011.
 36. Eshtehardi P, McDaniel MC, Suo J, Dhawan SS, Timmins LH, Binongo JNG, Golub LJ, Corban MT, Finn A V., Oshinsk JN, Quyyumi AA, Giddens DP, Samady H. Association of Coronary Wall Shear Stress With Atherosclerotic Plaque Burden, Composition, and Distribution in Patients With Coronary Artery Disease. *Journal of the American Heart Association*. 2012.
 37. Arzani A, Suh GY, Dalman RL, Shadden SC. A longitudinal comparison of hemodynamics and intraluminal thrombus deposition in abdominal aortic aneurysms. *American Journal of Physiology - Heart and Circulatory Physiology*. 2014.
 38. Shojima M, Oshima M, Takagi K, Torii R, Hayakawa M, Katada K, Morita A, Kirino T. Magnitude and role of wall shear stress on cerebral aneurysm: Computational fluid

dynamic study of 20 middle cerebral artery aneurysms. In: *Stroke*.; 2004.

39. Fujimoto M, Shobayashi Y, Tateshima S, Sudo R, Tanishita K, Viñuela F. Comparison of simulated structural deformation with experimental results after Wingspan stenting. *Neurological Research*. 2014;36(8):752–756.
40. Gundert TJ, Shadden SC, Williams AR, Koo BK, Feinstein JA, Ladisa JF. A rapid and computationally inexpensive method to virtually implant current and next-generation stents into subject-specific computational fluid dynamics models. *Annals of Biomedical Engineering*. 2011;39(5):1423–1437.
41. Chiastra C, Wu W, Dickerhoff B, Aleiou A, Dubini G, Otake H, Migliavacca F, LaDisa JF. Computational replication of the patient-specific stenting procedure for coronary artery bifurcations: From OCT and CT imaging to structural and hemodynamics analyses. *Journal of Biomechanics*. 2016;49(11):2102–2111.
42. Eslami P, Tran J, Jin Z, Karady J, Sotoodeh R, Lu MT, Hoffmann U, Marsden A. Effect of Wall Elasticity on Hemodynamics and Wall Shear Stress in Patient-Specific Simulations in the Coronary Arteries. *Journal of Biomechanical Engineering*. 2020;142(2).
43. Li L, Terry CM, Shiu YTE, Cheung AK. Neointimal hyperplasia associated with synthetic hemodialysis grafts. *Kidney International*. 2008.
44. Moore JE, Xu C, Glagov S, Zarins CK, Ku DN. Fluid wall shear stress measurements in a model of the human abdominal aorta: oscillatory behavior and relationship to atherosclerosis. *Atherosclerosis*. 1994.
45. Hardman D, Semple SI, Richards JMJ, Hoskins PR. Comparison of patient-specific inlet boundary conditions in the numerical modelling of blood flow in abdominal aortic aneurysm disease. *International Journal for Numerical Methods in Biomedical Engineering*. 2013.
46. Patricio L, Tonino PAL, De Bruyne B, Pijls NHJ, Siebert U, Ikeno F, Van Veer MT, Klauss V, Manoharan G, Engstrøm T, Oldroyd KG, Lee PN Ver, MacCarthy PA, Fearon WF. Fractional flow reserve versus angiography for guiding percutaneous coronary intervention. *Revista Portuguesa de Cardiologia*. 2009.
47. Zimmermann FM, De Bruyne B, Pijls NHJ, Desai M, Oldroyd KG, Park SJ, Reardon MJ, Wendler O, Woo J, Yeung AC, Fearon WF. Rationale and design of the Fractional Flow Reserve versus Angiography for Multivessel Evaluation (FAME) 3 Trial: A comparison of fractional flow reserve-guided percutaneous coronary intervention and coronary artery bypass graft surgery in patients with m. *American Heart Journal*. 2015.
48. Katritsis D, Pantos I. Fractional flow reserve derived from coronary imaging and computational fluid dynamics. *Interventional Cardiology Review*. 2014;9(3):145–150.
49. Pocock S, Quirós A, Echavarría-Pinto M, van de Hoef TP, van Lavieren MA, Meuwissen M, Serruys PW, Escaned J, Macaya C, Ibañez B, Davies J, Piek JJ, Nijjer S. Combining Baseline Distal-to-Aortic Pressure Ratio and Fractional Flow Reserve in the Assessment of Coronary Stenosis Severity. *JACC: Cardiovascular Interventions*. 2015;8(13):1681–1691.

50. Bressi E, Mangiacapra F, Morisco C, Barbato E, Sticchi A. Fractional flow reserve (FFR) as a guide to treat coronary artery disease. *Expert Review of Cardiovascular Therapy*. 2018;16(7):465–477.
51. Zimmermann FM, Kobayashi Y, Mullen WL, Fearon WF. Non-invasive FFR CT revealing severe inducible ischaemia in an anomalous right coronary artery. *European Heart Journal*. 2017.
52. Koo BK, Erglis A, Doh JH, Daniels D V., Jegere S, Kim HS, Dunning A, Defrance T, Lansky A, Leipsic J, Min JK. Diagnosis of ischemia-causing coronary stenoses by noninvasive fractional flow reserve computed from coronary computed tomographic angiograms: Results from the prospective multicenter DISCOVER-FLOW (Diagnosis of Ischemia-Causing Stenoses Obtained Via Noni. *Journal of the American College of Cardiology*. 2011.
53. Hulten E, Blankstein R, Di Carli MF. The value of noninvasive computed tomography derived fractional flow reserve in our current approach to the evaluation of coronary artery stenosis. *Current Opinion in Cardiology*. 2016;31(6):670–676.
54. Gonzalez JA, Lipinski MJ, Flors L, Shaw PW, Kramer CM, Salerno M. Meta-analysis of diagnostic performance of coronary computed tomography angiography, computed tomography perfusion, and computed tomography-fractional flow reserve in functional myocardial ischemia assessment versus invasive fractional flow reserve. *American Journal of Cardiology*. 2015.
55. Sambuceti G, Marzilli M, Fedele S, Marini C, Abbate AL. Paradoxical Increase in Microvascular Resistance During Tachycardia Downstream From a Severe Stenosis in. *World Wide Web Internet And Web Information Systems*. 2001:2352–2360.
56. Guarini G, Capozza PG, Huqi A, Morrone D, Chilian WM, Marzilli M. Microvascular function/dysfunction downstream a coronary stenosis. *Current pharmaceutical design*. 2013;19(13):2366–74.
57. Van De Hoef TP, Nolte F, Echavarría-Pinto M, Van Lavieren MA, Damman P, Chamuleau SAJ, Voskuil M, Verberne HJ, Henriques JPS, Van Eck-Smit BLF, Koch KT, De Winter RJ, Spaan JAE, Siebes M, Tijssen JGP, et al. Impact of hyperaemic microvascular resistance on fractional flow reserve measurements in patients with stable coronary artery disease: Insights from combined stenosis and microvascular resistance assessment. *Heart*. 2014;100(12):951–959.
58. Garcia D, Harbaoui B, van de Hoef TP, Meuwissen M, Nijjer SS, Echavarria-Pinto M, Davies JE, Piek JJ, Lantelme P. Relationship between FFR, CFR and coronary microvascular resistance - Practical implications for FFR-guided percutaneous coronary intervention. *PloS one*. 2019;14(1):e0208612.
59. Kim HJ, Vignon-Clementel IE, Coogan JS, Figueroa CA, Jansen KE, Taylor CA. Patient-specific modeling of blood flow and pressure in human coronary arteries. *Annals of Biomedical Engineering*. 2010;38(10):3195–3209.
60. Sengupta D, Kahn AM, Burns JC, Sankaran S, Shadden SC, Marsden AL. *Image-based*

modeling of hemodynamics in coronary artery aneurysms caused by Kawasaki disease.; 2012.

61. Williams AR, Koo B-K, Gundert TJ, Fitzgerald PJ, LaDisa JF. Local hemodynamic changes caused by main branch stent implantation and subsequent virtual side branch balloon angioplasty in a representative coronary bifurcation. *Journal of Applied Physiology*. 2010;109(2):532–540.
62. Burattini R, Sipkema P, van Huis G a, Westerhof N. Identification of canine coronary resistance and intramyocardial compliance on the basis of the waterfall model. *Annals of biomedical engineering*. 1985;13(5):385–404.
63. Van Huis G a, Sipkema P, Westerhof N. Coronary input impedance during cardiac cycle as determined by impulse response method. *The American journal of physiology*. 1987;253(2 Pt 2):H317-24.
64. Arthurs CJ, Lau KD, Asrress KN, Redwood SR, Figueroa CA. A mathematical model of coronary blood flow control: simulation of patient-specific three-dimensional hemodynamics during exercise. *American Journal of Physiology - Heart and Circulatory Physiology*. 2016;310(9):H1242–H1258.
65. Virmani R, Chun PKC, Goldstein RE, Robinowitz M, Mcallister HA. Acute takeoffs of the coronary arteries along the aortic wall and congenital coronary ostial valve-like ridges: Association with sudden death. *Journal of the American College of Cardiology*. 1984;3(3):766–771.
66. LaDisa JF, Alberto Figueroa C, Vignon-Clementel IE, Jin Kim H, Xiao N, Ellwein LM, Chan FP, Feinstein JA, Taylor CA. Computational Simulations for Aortic Coarctation: Representative Results From a Sampling of Patients. *Journal of Biomechanical Engineering*. 2011;133(9):091008.
67. Stergiopoulos N, Segers P, Westerhof N. Use of pulse pressure method for estimating total arterial compliance in vivo. *American Journal of Physiology-Heart and Circulatory Physiology*. 1999;276(2):H424–H428.
68. Spaan JAE. Coronary diastolic pressure-flow relation and zero flow pressure explained on the basis of intramyocardial compliance. *Circulation Research*. 1985;56(3):293–309.
69. L. E, J.F. L, S. L, S. S-I. Quantification of thoracic aorta blood flow by magnetic resonance imaging during supine cycling exercise of increasing intensity. *Journal of Cardiovascular Magnetic Resonance*. 2013;15(SUPPL. 1):391.
70. Hayabuchi Y, Ono A, Homma Y, Kagami S. Analysis of right ventricular myocardial stiffness and relaxation components in children and adolescents with pulmonary arterial hypertension. *Journal of the American Heart Association*. 2018;7(9):1–11.
71. Wong J, Pushparajah K, De Vecchi A, Greil GF, Hussain T, Razavi R. Myocardial contractile response to dobutamine in hypoplastic left heart syndrome post-Fontan. *Journal of Cardiovascular Magnetic Resonance*. 2014;16(Suppl 1):O104.
72. Mitchell JR, Wang J-J. Expanding application of the Wiggers diagram to teach cardiovascular physiology. *Advances in Physiology Education*. 2014;38(2):170–175.

73. Åstrand P-O, Rodahl K. *Textbook of work physiology : physiological bases of exercise*. McGraw-Hill; 1977.
74. Stergiopoulos N, Segers P, Westerhof N. Use of pulse pressure method for estimating total arterial compliance in vivo. *American Journal of Physiology-Heart and Circulatory Physiology*. 1999;276(2):H424–H428.
75. Zamir M, Sinclair P, Wonnacott TH. Relation between diameter and flow in major branches of the arch of the aorta. *Journal of Biomechanics*. 1992;25(11):1303–1310.
76. Milnor WR. *Cardiovascular physiology*. New York : Oxford University Press; 1990.
77. Iskandrian AS, Verani MS, Heo J. Pharmacologic stress testing: Mechanism of action, hemodynamic responses, and results in detection of coronary artery disease. *Journal of Nuclear Cardiology*. 1994;1(1):94–111.
78. Stephens J, Ead H, Spurrell R. Haemodynamic effects of dobutamine with special reference to myocardial blood flow A comparison with dopamine and isoprenaline. 1979:43–50.
79. Beanlands RSB, Bach DS, Raylman R, Armstrong WF, Wilson V, Montieth M, Moore CK, Bates E, Schwaiger M. Acute effects of dobutamine on myocardial oxygen consumption and cardiac efficiency measured using carbon-11 acetate kinetics in patients with dilated cardiomyopathy. *Journal of the American College of Cardiology*. 1993;22(5):1389–1398.
80. Lee J, Chae SC, Lee K, Heo J, Iskandrian AS. Biokinetics of thallium-201 in normal subjects: comparison between adenosine, dipyridamole, dobutamine and exercise. *J Nucl Med*. 1994;35(4):535–541.
81. Chilian WM, Layne SM, Klausner EC, Eastham CL, Marcus ML. Redistribution of coronary microvascular resistance produced by dipyridamole. *The American journal of physiology*. 1989;256(2):H383-90.
82. Chilian WM, Layne SM. Heterogenous Microvascular Coronary α -Adrenergic Vasoconstriction. *Circulation Research*. 1989;64:376.
83. Coogan JS, Humphrey JD, Figueroa CA. Computational simulations of hemodynamic changes within thoracic, coronary, and cerebral arteries following early wall remodeling in response to distal aortic coarctation. *Biomechanics and Modeling in Mechanobiology*. 2013;12(1):79–93.
84. Manor D, Sideman S, Dinnar U, Beyar R. Analysis of flow in coronary epicardial arterial tree and intramyocardial circulation. *Medical and Biological Engineering and Computing*. 1994;32(1):S133–S143.
85. Noto N, Ayusawa M, Karasawa K, Yamaguchi H, Sumitomo N, Okada T, Harada K. Dobutamine stress echocardiography for detection of coronary artery stenosis in children with Kawasaki disease. *Journal of the American College of Cardiology*. 1996;27(5):1251–1256.

86. Boutouyrie P, Lacolley P, Girerd X, Beck L, Safar M, Laurent S. Sympathetic activation decreases medium-sized arterial compliance in humans. *American Journal of Physiology-Heart and Circulatory Physiology*. 1994;267(4):H1368–H1376.
87. Tune JD, Richmond KN, Gorman MW, Feigl EO. Control of Coronary Blood Flow during Exercise. *Experimental Biology and Medicine*. 2002;227(4):238–250.
88. Chilian WM, Marcus ML. Effects of coronary and extravascular pressure on intramyocardial and epicardial blood velocity. *The American journal of physiology*. 1985;248(2 Pt 2):H170-8.
89. Kajiyama F, Tsujioka K, Goto M, Wada Y, Chen XL, Nakai M, Tadaoka S, Hiramatsu O, Ogasawara Y, Mito K. Functional characteristics of intramyocardial capacitance vessels during diastole in the dog. *Circulation Research*. 1986;58(4):476–485.
90. SALISBURY PF, CROSS CE, RIEBEN PA. Intramyocardial pressure and strength of left ventricular contraction. *Circulation research*. 1962;10:608–623.
91. Stein PD, Sabbah HN, Marzilli M, Blick EF. Comparison of the distribution of intramyocardial pressure across the canine left ventricular wall in the beating heart during diastole and in the arrested heart. Evidence of epicardial muscle tone during diastole. *Circulation Research*. 1980;47(2):258–267.
92. Stein PD, Sabbah HN, Marzilli M. Intramyocardial Pressure and Coronary Extravascular Resistance. *Journal of Biomechanical Engineering*. 1985;107(1):46–50.
93. Schreiner W, Neumann F, Mohl W. The role of intramyocardial pressure during coronary sinus interventions: A computer model study. *IEEE Transactions on Biomedical Engineering*. 1990;37(10):956–967.
94. Brooks H, Kirk ES, Vokonas PS, Urschel CW, Sonnenblick EH. Performance of the right ventricle under stress: relation to right coronary flow. *The Journal of clinical investigation*. 1971;50(10):2176–2183.
95. Dunaway S, Yu Q, Larson DF. Effect of acute alpha adrenergic stimulation on cardiac function. *Perfusion*. 2007;22(4):289–292.
96. Friedman BJ, Lozner EC, Curfman GD, Herzberg D, Rolett EL. Characterization of the human right ventricular pressure-volume relation: Effect of dobutamine and right coronary artery stenosis. *Journal of the American College of Cardiology*. 1984;4(5):999–1005.
97. Bovendeerd PHM, Borsje P, Arts T, Van De Vosse FN. Dependence of intramyocardial pressure and coronary flow on ventricular loading and contractility: A model study. *Annals of Biomedical Engineering*. 2006;34(12):1833–1845.
98. Mihailescu LS, Abel FL. Intramyocardial pressure gradients in working and nonworking isolated cat hearts. *American Journal of Physiology*. 1994;266(3 Pt 2):H1233–H1241.
99. Fernholz H-H. Boundary Layer Theory. *European Journal of Mechanics - B/Fluids*. 2001;20(1):155–157.

100. Caballero AD, Laín S. Numerical simulation of non-Newtonian blood flow dynamics in human thoracic aorta. *Computer Methods in Biomechanics and Biomedical Engineering*. 2015;18(11):1200–1216.
101. Vignon-Clementel IE, Alberto Figueroa C, Jansen KE, Taylor CA. Outflow boundary conditions for three-dimensional finite element modeling of blood flow and pressure in arteries. *Computer Methods in Applied Mechanics and Engineering*. 2006.
102. Razavi A, Shirani E, Sadeghi MR. Numerical simulation of blood pulsatile flow in a stenosed carotid artery using different rheological models. *Journal of Biomechanics*. 2011;44(11).
103. Zamir M. Shear forces and blood vessel radii in the cardiovascular system. *Journal of General Physiology*. 1977;69(4):449–461.
104. de Winter JCF, Winter JCF De, de Winter JCF. Using the Student 's t -test with extremely small sample sizes. *Practical Assessment, Research & Evaluation*. 2013;18(10):1–12.
105. Jegatheeswaran A, Devlin PJ, McCrindle BW, Williams WG, Jacobs ML, Blackstone EH, DeCampli WM, Caldarone CA, Gaynor JW, Kirklin JK, Lorber RO, Mery CM, St. Louis JD, Molossi S, Brothers JA. Features associated with myocardial ischemia in anomalous aortic origin of a coronary artery: A Congenital Heart Surgeons' Society study. *Journal of Thoracic and Cardiovascular Surgery*. 2019.
106. Maria Formato G, Lo Rito M, Auricchio F, Frigiola A, Conti M. Aortic Expansion Induces Lumen Narrowing in Anomalous Coronary Arteries: A Parametric Structural Finite Element Analysis. *Journal of Biomechanical Engineering*. 2018;140(11):111008.
107. Krupiński M, Urbańczyk-Zawadzka M, Laskowicz B, Irzyk M, Banyś R, Klimeczek P, Gruszczyńska K, Baron J. Anomalous origin of the coronary artery from the wrong coronary sinus evaluated with computed tomography: “High-risk” anatomy and its clinical relevance. *European Radiology*. 2014;24(10):2353–2359.
108. Marcus TT, Smeenk HG, Kuijter JPA, Van Der Geest RJ, Heethaar RM, Van Rossum AC. Flow profiles in the left anterior descending and the right coronary artery assessed by MR velocity quantification: Effects of through-plane and in-plane motion of the heart. *Journal of Computer Assisted Tomography*. 1999.
109. Boussel L, Rayz V, McCulloch C, Martin A, Acevedo-Bolton G, Lawton M, Higashida R, Smith WS, Young WL, Saloner D. Aneurysm growth occurs at region of low wall shear stress: Patient-specific correlation of hemodynamics and growth in a longitudinal study. *Stroke*. 2008.
110. Bonert M, Leask RL, Butany J, Ethier CR, Myers JG, Johnston KW, Ojha M. The relationship between wall shear stress distributions and intimal thickening in the human abdominal aorta. *BioMedical Engineering Online*. 2003.
111. Brothers JA, Kim TS, Fogel MA, Whitehead KK, Morrison TM, Paridon SM, Harris MA. Cardiac magnetic resonance imaging characterizes stenosis, perfusion, and fibrosis preoperatively and postoperatively in children with anomalous coronary arteries. *Journal of Thoracic and Cardiovascular Surgery*. 2016.

112. Zhou Y, Kassab GS, Molloy S. Contact us My IOPscience On the design of the coronary arterial tree : a generalization of Murray ' s law On the design of the coronary arterial tree : a generalization of Murray ' s law. *Sciences-New York*. 1999;2929:2929–2945.
113. Alqarqaz M, Basir M, Alaswad K, O'Neill W. Effects of Impella on Coronary Perfusion in Patients With Critical Coronary Artery Stenosis. *Circulation: Cardiovascular Interventions*. 2018;11(4):1–8.
114. Papaioannou TG, Stefanadis C. Vascular wall shear stress: Basic principles and methods. *Hellenic Journal of Cardiology*. 2005.
115. Van De Hoef TP, Meuwissen M, Escaned J, Davies JE, Siebes M, Spaan JAE, Piek JJ. Fractional flow reserve as a surrogate for inducible myocardial ischaemia. *Nature Reviews Cardiology*. 2013.
116. Figueroa CA, Vignon-Clementel IE, Jansen KE, Hughes TJR, Taylor CA. A coupled momentum method for modeling blood flow in three-dimensional deformable arteries. *Computer Methods in Applied Mechanics and Engineering*. 2006.
117. Kandail HS, Trivedi SD, Shaikh AC, Bajwa TK, O'Hair DP, Jahangir A, LaDisa JF. Impact of annular and supra-annular CoreValve deployment locations on aortic and coronary artery hemodynamics. *Journal of the Mechanical Behavior of Biomedical Materials*. 2018;86(June):131–142.
118. Weissman NJ, Palacios IF, Weyman AE. Dynamic expansion of the coronary arteries: Implications for intravascular ultrasound measurements. *American Heart Journal*. 1995.
119. Santamarina a, Weydahl E, Siegel JM, Moore JE. of the Coronary Arteries : Effects of Time-varying Curvature. *Annals of Biomedical Engineering*. 1998;26:944–954.
120. Zeng D, Ding Z, Friedman MH, Ross Ethier C. Effects of cardiac motion on right coronary artery hemodynamics. *Annals of Biomedical Engineering*. 2003;31(4):420–429.
121. Zeng D, Boutsianis E, Ammann M, Boomsma K, Wildermuth S, Poulikakos D. A Study on the Compliance of a Right Coronary Artery and Its Impact on Wall Shear Stress. *Journal of Biomechanical Engineering*. 2008;130(4):041014.
122. Wendell DC, Samyn MM, Cava JR, Ellwein LM, Krolikowski MM, Gandy KL, Pelech AN, Shadden SC, LaDisa JF. Including aortic valve morphology in computational fluid dynamics simulations: Initial findings and application to aortic coarctation. *Medical Engineering and Physics*. 2013.
123. Youssefi P, Gomez A, Arthurs C, Sharma R, Jahangiri M, Figueroa CA. Impact of patient-specific inflow velocity profile on hemodynamics of the thoracic aorta. *Journal of Biomechanical Engineering*. 2018.
124. Bertelsen L, Svendsen JH, Køber L, Haugan K, Højberg S, Thomsen C, Vejlstrup N. Flow measurement at the aortic root - Impact of location of through-plane phase contrast velocity mapping. *Journal of Cardiovascular Magnetic Resonance*. 2016.

125. De Nisco G, Hoogendoorn A, Chiastra C, Gallo D, Kok AM, Morbiducci U, Wentzel JJ. The impact of helical flow on coronary atherosclerotic plaque development. *Atherosclerosis*. 2020.
126. Hoogendoorn A, Kok AM, Hartman EMJ, de Nisco G, Casadonte L, Chiastra C, Coenen A, Korteland S-A, Van der Heiden K, Gijzen FJH, Duncker DJ, van der Steen AFW, Wentzel JJ. Multidirectional wall shear stress promotes advanced coronary plaque development: comparing five shear stress metrics. *Cardiovascular Research*. 2019.